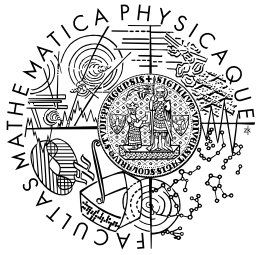

FACULTY
OF MATHEMATICS
AND PHYSICS
Charles University

MASTER THESIS

Zuzana Procházková

On the Internal Gravity Wave - Atmospheric Circulation Interaction

Department of Atmospheric Physics

Supervisor of the master thesis: RNDr. Petr Šácha, Ph.D.

Study programme: Physics

Study branch: Mathematical and Computer Modelling in Physics

Prague 2021

I declare that I carried out this master thesis independently, and only with the cited sources, literature and other professional sources. It has not been used to obtain another or the same degree.

I understand that my work relates to the rights and obligations under the Act No. 121/2000 Sb., the Copyright Act, as amended, in particular the fact that the Charles University has the right to conclude a license agreement on the use of this work as a school work pursuant to Section 60 subsection 1 of the Copyright Act.

In Čechtice, 20$^{\text{th}}$ May 2021 Zuzana Procházková

I would like to thank my supervisor RNDr. Petr Šácha, Ph.D. for his kind guidance and time. Special thanks go also to my consultants Mgr. Aleš Kuchař, Ph.D., doc. RNDr. Petr Pišoft, Ph.D. and Mgr. Vít Průša, Ph.D. for their advice. Finally, I would like to express my gratitude to Dr. Christopher Kruse for providing the data. The thesis was supported by GAUK 281021.

Title: On the Internal Gravity Wave - Atmospheric Circulation Interaction

Author: Zuzana Procházková

Department: Department of Atmospheric Physics

Supervisor: RNDr. Petr Šácha, Ph.D., Department of Atmospheric Physics

Abstract: Internal gravity waves (GWs) are an important component of the atmospheric dynamics, significantly affecting the middle atmosphere by momentum and energy transport and deposition. In order to be able to improve global circulation models, in which the majority of the GW spectrum is not resolved, it is necessary to quantify their effects as precise as possible. We study GWs in a high-resolution simulation of the WRF model around Southern Andes, Antarctic Peninsula and South Georgia Island. We analyse a Gaussian high-pass filter method for separation of the GWs from the basic flow. To overcome an observed problem of dependence of the method on a cutoff parameter, we propose an improved method that determines the parameter at each time step from the horizontal kinetic energy spectrum. The differences between the methods are further examined using the horizontal kinetic energy spectrum, vertical potential energy spectrum and forcing to the divergence equation evaluated by the active wind method, which is a recent theory-based method that divides the flow into a balanced flow and a perturbation field. The results suggest that the high-pass filter method does not produce correct results for time periods with strong wave activity.

Keywords: internal gravity waves, momentum flux, general stationary solution, high resolution model simulations

Contents

Introduction

Internal gravity waves (GWs) manifest themselves in the flow as oscillations driven by the buoyancy force within the fluid [1],[2]. One of their crucial properties is the variety of temporal and spatial scales on which they emerge. Horizontal wavelengths of GWs range from thousands to a few kilometers [3]. They dominate the mesoscale wave spectrum (wavelengths in the orders of 10 - 1000 km) in the middle atmosphere [4] but they also impact the synoptic scale [5] and planetary scale circulations [4]. They can also directly influence the surface weather conditions including extreme weather events. For example, mountain waves, which belong to gravity waves, can support the development of strong warm Foehn winds [6].

The fact that the internal gravity waves exist on greater range of scales presents a challenge for numerical atmospheric models, as the scale of a significant portion of the GW spectrum is smaller than the scale of the computational grid. Even if the resolution of the model is experimentally set higher, it seems that the result still miss important GW effects [7]. The problem is bypassed by using so-called parameterizations that supplement the influence of sub-grid scale processes in order to get realistic wind and temperature climatologies in the models.

GW parameterization schemes employ various simplifications of the sourcing, propagation and dissipation processes. Usually, the schemes assume linear, hydrostatic, vertically propagating GWs. In the level of GWs saturation, the schemes decelerate the resolved flow in the model [8]. The parameterizations employ several tunable parameters that are set so that the model is in agreement with observed temperature and wind climatologies [9] or with some more complex atmospheric phenomena concerning middle-atmosphere variability such as quasi-biennial oscillation [10] or frequency of sudden stratospheric warming [11].

Constraining the tunable parameters is complicated, because it requires general knowledge of GW features like the global distribution of wavelengths, frequencies or momentum fluxes of the waves [12]. Because GWs act on various spatio-temporal scales, observing them in the real atmosphere is not an easy task.

In principle, the momentum flux can be measured using satellite methods, superpressure balloons or radiosondes [9]. The satellite measurements use the fact that the magnitude of the momentum flux is proportional to the temperature, which can be measured very precisely. Due to the fact that only a part of the GW spectrum is sampled, the dependence of the horizontal resolution on the measurement track, and many approximations made during the post-processing of the data such as single wave assumption or mid frequency approximation, satellite measurements result in relatively high error in the propagation direction and wavelength [13].

Observations by superpressure balloons can supplement the very uncertain information from satellite measurements, as the balloons measure horizontal temperature and pressure anomalies with great precision while drifting with the wind. On the other hand, the balloons provide information that is horizontally sparse and for a given altitude only [14], [15].

Using the radiosonde data, it is also possible to combine temperature and

wind information to obtain GW momentum fluxes [16]. However, the methods computing momentum flux that use the radiosonde data do not cover whole gravity wave spectrum [9] and the information is purely local. Another option are in situ radars and lidars.

All in all, observational estimates of GW parameters and their momentum fluxes and resulting drag include significant uncertainty. To be able to constrain GW parametrisation in the global circulation models, it is necessary to obtain the information by other means. Therefore, it seems reasonable to first utilize models with very high resolution, which would allow us to simulate the majority of the GW spectrum, and then use the knowledge to improve existing parametrisations.

In the thesis, we study the GWs and their interaction with background flow using experimental model runs of Weather Research and Forecasting Model with horizontal resolution of 3 km. We discuss different methods for GW detection and we apply two of them – a high-pass filter method and a method based on a division of the flow to so-called active and inactive components. We study the properties of the methods and the spectrum of the gravity waves present in the data.

In Chapter 1, we introduce the internal gravity waves and we derive some of their properties. In Chapter 2, the theoretical concepts used on the gravity wave detection and analysis are presented. Chapter 3 contains an analysis of the results of our computations on the model data.

1. Waves in the Atmosphere

The circulation of the air in the atmosphere consists of a variety of motion types. Apart from the patterns given by the global atmospheric circulations, it is possible to observe diverse wave-like motions. They differ in the mechanism of origin, scale at which they occur and their propagation speed. Some of them are described in the first part of this chapter. In the second part of the chapter, we describe the internal gravity waves, which are the waves studied in the thesis.

1.1 Some Basic Wave Types

The waves with the shortest period are the **sound waves** [2]. They show itself as a regular compression and rarefaction of the air. Because they propagate relatively quickly, they might cause a problem with the convergence of an atmospheric model due to the Courant–Friedrichs–Lewy condition. To improve the model convergence, sound waves can be excluded by assuming the incompressibility of the air. A similar sound wave filtering effect is also caused by the hydrostatic approximation, by which the pressure can depend on the height only.

The other wave motions can be divided into two parts. In the first type of wave motions, an initial perturbation is propagated as a consequence of the rotation of the Earth. In the second type, the conditions for the propagation of an initial perturbation are caused by the stratification of the fluid, i.e. its inhomogeneity. Regarding the waves driven by the Earth rotation, we will mention inertial oscillations, Rossby waves and Kelvin waves.

The simplest type of the wave motion related to the Earth rotation are the **inertial oscillations** [17] that describe a circular motion of a free particle on the rotating Earth. The period and radius of the inertial oscillations is interconnected with the period of Earth rotation.

Another important wave type are the **Rossby waves** [2]. In a simplified setting, they result from the conservation of absolute vorticity and from the fact that the Coriolis parameter depends on latitude. Rossby waves can arise in the westerly flow only and they lead to horizontal meandering of the flow. They can be easily observed as meanders of the tubes of very strong wind, of jet streams. In case of strong amplitudes, Rossby waves can give rise to the cyclons and anticyclones, which has a significant influence on the weather.

Kelvin waves are waves that also emerge because of the Coriolis effect. Nevertheless, for these waves a lateral boundary is needed. Kelvin waves are therefore often described for the ocean near coastlines. They can, however, also appear in the equatorial zone of the atmosphere, where the equator plays the role of the boundary [2].

As the first example of waves that emerge because of stratification, we can consider a boundary between two air masses with different properties. If the boundary contains discontinuity in the density and sufficiently large discontinuity in the velocity, along the interface then originate waves called **Kelvin-Helmholtz waves** [18]. In case the waves are accompanied by lifting of a moist so that the water condense, characteristic clouds can be observed.

1.2 Internal Gravity Waves

The waves propagating inside a fluid mass that are based on the stratification are called the internal gravity waves. They are basically oscillations emerging as a result of the buoyancy force from an initial perturbation.

The initial perturbation can occur in the atmosphere for different reasons, for example because of the convection, wind shear or interaction with other waves [3]. In this thesis, we deal with the internal gravity waves resulting from the flow over topography.

Similarly to the sound waves, in the atmospheric models, the internal gravity waves can be partially eliminated by the hydrostatic approximation. Because they act on small scales, part of their spectrum is also not resolved by the models. Nevertheless, the internal gravity waves significantly impact the middle atmosphere by the momentum and energy transport and deposition and their effects must be supplied to the models.

In the following sections, we first illustrate the mechanism of the internal gravity waves on the stability description of vertical oscillation. Afterwards, we derive the dispersion relation that shows the relation of gravity wave frequency and wavenumbers in the frame of linear perturbation theory.

1.2.1 Vertical Oscillation

A simplified concept of the internal gravity waves can be presented by considering the vertical oscillation of a fluid parcel [6].

First, we consider motionless fluid with density $\bar{\rho}(z)$ depending on the height only. At the height z_0, the density of the fluid is $\rho_0 = \bar{\rho}(z_0)$. Next, we select a fluid parcel at the height z_0 and move it up to the height $z_0 + \Delta z$. A fluid particle is a part of the fluid, which is sufficiently small so that it can be moved without causing any motion of the surrounding fluid.

For simplicity, we assume that the density of the parcel ρ_0 does not change during the shifting. The density of the ambient fluid, however, changes to the value $\bar{\rho}(z_0+\Delta z)$. This generates the difference of the fluid parcel and the ambient flow $\Delta\bar{\rho}$ that can be approximated by writing

$$\Delta\bar{\rho} = \rho_0 - \bar{\rho}(z_0 + \Delta z) = \bar{\rho}(z_0) - \bar{\rho}(z_0 + \Delta z) \approx -\left.\frac{\mathrm{d}\bar{\rho}}{\mathrm{d}z}\right|_{z=z_0} \Delta z. \tag{1.1}$$

The density difference further generates the buoyancy force per volume acting on the particle, which equals $-g\Delta\bar{\rho}$. By the second Newton's law, the time evolution of the vertical displacement Δz is given by equation

$$\rho_0 \frac{\mathrm{d}^2(\Delta z)}{\mathrm{d}t^2} = -g\Delta\bar{\rho}. \tag{1.2}$$

After inserting the term $\Delta\bar{\rho}$ from equation (1.1), we immediately get

$$\frac{\mathrm{d}^2(\Delta z)}{\mathrm{d}t^2} - \frac{g}{\rho_0}\left.\frac{\mathrm{d}\bar{\rho}}{\mathrm{d}z}\right|_{z=z_0} \Delta z = 0. \tag{1.3}$$

This equation can be written in the form

$$\frac{\mathrm{d}^2(\Delta z)}{\mathrm{d}t^2} + N^2(z_0)\Delta z = 0, \tag{1.4}$$

which is the harmonic oscillator equation for a fluid parcel starting at the height z_0 that starts oscillating with the frequency N given by the formula

$$N^2 = -\frac{g}{\bar{\rho}}\frac{\mathrm{d}\bar{\rho}}{\mathrm{d}z}. \tag{1.5}$$

The spring equation is an equation that could have been anticipated for the motion of a fluid parcel deflected from its equilibrium position. However, for the motion of the air in the atmosphere, the assumption on the density of the particle being constant during the motion is rather unrealistic.

Instead, it is reasonable to assume that the air parcel moves adiabatically. In this case, we can assume the conservation of a quantity called the potential temperature instead of the conservation of the density, because the potential temperature is defined as the temperature of a fluid parcel that was brought adiabatically to a certain pressure level.

Such a change affects the definition of the frequency N in equation (1.4). After expressing the dependence of background density on the background potential temperature $\bar{\theta}$ in the hydrostatic balance [6], it is possible to get the same spring equation as before with the frequency given by the formula

$$N^2 = \frac{g}{\bar{\theta}}\frac{\mathrm{d}\bar{\theta}}{\mathrm{d}z}. \tag{1.6}$$

The frequency N defined by equation (1.6) is called the Brunt-Väisälä frequency. It is a basic quantity for the description of the atmospheric stability of stratification. If it holds that $N^2 > 0$, i.e. the potential temperature increases with height, the atmosphere is said to be atmospheric stable. In this case, in view of equation (1.4), the internal gravity waves can be present in the atmosphere. On the other hand, if $N^2 < 0$, the atmosphere is unstable, and the internal gravity waves cannot exist in this part of the atmosphere.

1.2.2 Dispersion and Polarization Relations

To understand the propagation of the internal gravity waves, following [3], we derive their dispersion relation, which is an equation that relates the wave frequency to its spatial characteristics. Also, we show an example of a polarization relation, which connects the amplitudes of different quantities.

Similarly to above, we divide the flow to the horizontal uniform basic flow in hydrostatic equilibrium and a linear perturbation. The problem is here nevertheless studied in the Eulerian frame.

The flow of the air in the atmosphere without external forcing can be described

by equations

$$\frac{\mathrm{d}u}{\mathrm{d}t} = -\frac{1}{\rho}\frac{\partial p}{\partial x} + fv, \tag{1.7a}$$

$$\frac{\mathrm{d}v}{\mathrm{d}t} = -\frac{1}{\rho}\frac{\partial p}{\partial y} - fu, \tag{1.7b}$$

$$\frac{\mathrm{d}w}{\mathrm{d}t} = -\frac{1}{\rho}\frac{\partial p}{\partial z} - g, \tag{1.7c}$$

$$\frac{\mathrm{d}\rho}{\mathrm{d}t} = -\rho\left(\frac{\partial u}{\partial x} + \frac{\partial v}{\partial y} + \frac{\partial w}{\partial z}\right), \tag{1.7d}$$

$$\frac{\mathrm{d}\theta}{\mathrm{d}t} = 0. \tag{1.7e}$$

The first three equations represent conservation of linear momentum, where u, v and w are the velocity components, p is the pressure and f is the Coriolis parameter. The fourth equation for the density ρ is the continuity equation. The last equation is the thermodynamic equation claiming the conservation of the potential temperature θ, as used in the previous section. The coordinates in which the equations are written are described in Attachment A. The system of equations is completed by adding the equation

$$\theta = \frac{p}{\rho R}\left(\frac{p_0}{p}\right)^{\kappa} \tag{1.8}$$

that connects the potential temperature with the pressure and density. The constant p_0 is a reference pressure value, R is the ideal gas constant and $\kappa = R/c_p$ with c_p the specific heat at constant pressure.

We assume the basic flow in the form $(\bar{u}(t,z), \bar{v}(t,z), 0)$, the potential temperature $\bar{\theta}(t,z)$, the pressure $\bar{p}(t,z)$ and the density $\bar{\rho}(t,z)$. The governing equations (1.7) for the basic flow therefore take form

$$\frac{\partial \bar{u}}{\partial t} = f\bar{v}, \tag{1.9a}$$

$$\frac{\partial \bar{v}}{\partial t} = -f\bar{u}, \tag{1.9b}$$

$$0 = -\frac{1}{\bar{\rho}}\frac{\partial \bar{p}}{\partial z} - g, \tag{1.9c}$$

$$\frac{\partial \bar{\rho}}{\partial t} = 0, \tag{1.9d}$$

$$\frac{\partial \bar{\theta}}{\partial t} = 0, \tag{1.9e}$$

$$\bar{\theta} = \frac{\bar{p}}{\bar{\rho}R}\left(\frac{p_0}{\bar{p}}\right)^{\kappa}. \tag{1.9f}$$

We further assume that the density $\bar{\rho}$ satisfies the equation

$$\bar{\rho} = \rho_0 \mathrm{e}^{-\frac{z-z_0}{H}}, \tag{1.10}$$

where ρ_0 is the value of density corresponding to a reference altitude z_0 and H is a constant parameter.

The perturbation of the basic flow is characterized by its velocity components u', v' and w', pressure p', density ρ' and potential temperature θ'. The decomposition of the flow into the basic flow and perturbation part can therefore be written as

$$u(t,x,y,z) = \bar{u}(t,z) + u'(t,x,y,z), \tag{1.11a}$$
$$v(t,x,y,z) = \bar{v}(t,z) + v'(t,x,y,z), \tag{1.11b}$$
$$w(t,x,y,z) = w'(t,x,y,z), \tag{1.11c}$$
$$p(t,x,y,z) = \bar{p}(t,z) + p'(t,x,y,z), \tag{1.11d}$$
$$\rho(t,x,y,z) = \bar{\rho}(t,z) + u'(t,x,y,z), \tag{1.11e}$$
$$\theta(t,x,y,z) = \bar{\theta}(t,z) + \theta'(t,x,y,z). \tag{1.11f}$$

Using the linear perturbation theory, we substitute the decomposition (1.11) into equation (1.7). The aim is to get linear equations for the variables u', v', w', $p'/\bar{\rho}$, $\rho'/\bar{\rho}$ and $\theta'/\bar{\rho}$, assuming that all the terms that are quadratic in the perturbation variables are negligible compared to the terms that are linear in the variables.

For example, for the first equation in (1.7), it is possible to write

$$\begin{aligned} 0 = \frac{\mathrm{d}u}{\mathrm{d}t} + \frac{1}{\rho}\frac{\partial p}{\partial x} - fv &= \frac{\partial\left(\bar{u}+u'\right)}{\partial t} + \left(\bar{u}+u'\right)\frac{\partial\left(\bar{u}+u'\right)}{\partial x} \\ &+ \left(\bar{v}+v'\right)\frac{\partial\left(\bar{u}+u'\right)}{\partial y} + w'\frac{\partial\left(\bar{u}+u'\right)}{\partial z} + \frac{1}{\bar{\rho}+\rho'}\frac{\partial\left(\bar{p}+p'\right)}{\partial x} - f\bar{v} - fv' \\ &= \frac{\partial u'}{\partial t} + \bar{u}\frac{\partial u'}{\partial x} + \bar{v}\frac{\partial u'}{\partial y} + w'\frac{\partial \bar{u}}{\partial z} + \frac{1}{\bar{\rho}}\frac{\partial p'}{\partial x} - fv' \end{aligned} \tag{1.12}$$

where we subtracted the first equation in (1.9) and used the fact that the basic flow does not depend on x and y.

Because the structure of derivatives that appeared in (1.12) will also reappear in other equations, it is reasonable to introduce a new derivative similar to the material derivative,

$$\frac{\mathrm{D}}{\mathrm{D}t} = \frac{\partial}{\partial t} + \bar{u}\frac{\partial}{\partial x} + \bar{v}\frac{\partial}{\partial y}. \tag{1.13}$$

The zonal momentum equation linearized in (1.12) can therefore be written compactly as

$$\frac{\mathrm{D}u'}{\mathrm{D}t} + w'\frac{\partial \bar{u}}{\partial z} + \frac{1}{\bar{\rho}}\frac{\partial p'}{\partial x} - fv' = 0. \tag{1.14}$$

In the same way, we can find the linearized version of the second governing equation in (1.7),

$$\frac{\mathrm{D}v'}{\mathrm{D}t} + w'\frac{\partial \bar{v}}{\partial z} + \frac{1}{\bar{\rho}}\frac{\partial p'}{\partial y} + fu' = 0. \tag{1.15}$$

In the third equation in (1.7), it is necessary to transform also the pressure gradient term, so that it contains the variable $p'/\bar{\rho}$:

$$\begin{aligned} 0 = \frac{\mathrm{d}w}{\mathrm{d}t} + \frac{1}{\rho}\frac{\partial p}{\partial z} + g &= \frac{\mathrm{D}w'}{\mathrm{D}t} + \frac{1}{\bar{\rho}+\rho'}\frac{\partial\left(\bar{p}+p'\right)}{\partial z} + g \\ &= \frac{\mathrm{D}w'}{\mathrm{D}t} - \frac{\bar{\rho}}{\bar{\rho}+\rho'}g + \frac{1}{\bar{\rho}+\rho'}\frac{\partial p'}{\partial z} + g. \end{aligned} \tag{1.16}$$

Using the density profile (1.10), the linearized equation is

$$\frac{\mathrm{D}w'}{\mathrm{D}t} + \frac{\rho'}{\bar{\rho}}g + \frac{\partial}{\partial z}\left(\frac{p'}{\bar{\rho}}\right) - \frac{1}{H}\frac{p'}{\bar{\rho}} = 0. \tag{1.17}$$

Similarly, the continuity equation and the equation for evolution of the potential temperature can be modified to

$$\frac{\mathrm{D}}{\mathrm{D}t}\left(\frac{\rho'}{\bar{\rho}}\right) + \frac{\partial u'}{\partial x} + \frac{\partial v'}{\partial y} + \frac{\partial w'}{\partial z} - \frac{1}{H}\frac{\rho'}{\bar{\rho}} = 0, \tag{1.18}$$

$$\frac{\mathrm{D}}{\mathrm{D}t}\left(\frac{\theta'}{\bar{\theta}}\right) + \frac{w'}{g}N^2 = 0, \tag{1.19}$$

with the Brunt-Väisälä frequency N defined consistently with the previous section as

$$N^2 = \frac{g}{\bar{\theta}}\frac{\partial\bar{\theta}}{\partial z}. \tag{1.20}$$

Finally, we rewrite equation (1.8). After subtracting the formula for the basic flow (1.9f) from the formula

$$\bar{\theta} + \theta' = \frac{\bar{p} + p'}{(\bar{\rho} + \rho')\,R}\left(\frac{p_0}{\bar{p} + p'}\right)^{\kappa}, \tag{1.21}$$

we get

$$\begin{aligned}\theta' &= \frac{p_0^{\kappa}}{R}\left(\frac{(\bar{p} + p')^{1-\kappa}}{\bar{\rho} + \rho'} - \frac{\bar{p}^{1-\kappa}}{\bar{\rho}}\right) = \frac{p_0^{\kappa}}{R}\frac{\bar{p}^{1-\kappa}}{\bar{\rho} + \rho'}\left(\frac{(\bar{p} + p')^{1-\kappa}}{\bar{p}^{1-\kappa}} - \frac{\bar{\rho} + \rho'}{\bar{\rho}}\right) \\ &= \frac{p_0^{\kappa}}{R}\frac{\bar{p}^{1-\kappa}}{\bar{\rho} + \rho'}\left(\left(1 + \frac{p'}{\bar{p}}\right)^{1-\kappa} - \left(1 + \frac{\rho'}{\bar{\rho}}\right)\right) \approx \bar{\theta}\left((1-\kappa)\frac{p'}{\bar{p}} - \frac{\rho'}{\bar{\rho}}\right).\end{aligned} \tag{1.22}$$

Using the notation for the speed of sound

$$c_s^2 = \frac{\bar{p}}{(1-\kappa)\bar{\rho}}, \tag{1.23}$$

we can therefore write the linearised version of equation (1.8) as

$$\frac{\theta'}{\bar{\theta}} = \frac{1}{c_s^2}\frac{p'}{\bar{\rho}} - \frac{\rho'}{\bar{\rho}}. \tag{1.24}$$

We now seek for a wave solution to the system of these six linearised equations. We proceed by assuming the form of the solution

$$\left(u', v', w', \frac{\theta'}{\bar{\theta}}, \frac{p'}{\bar{\rho}}, \frac{\rho'}{\bar{\rho}}\right) = \left(\tilde{u}, \tilde{v}, \tilde{w}, \tilde{\theta}, \tilde{p}, \tilde{\rho}\right)\exp\left[\mathrm{i}\,(kx + ly + mz - \omega t) + \frac{z}{2H}\right]. \tag{1.25}$$

The imaginary part of the exponential corresponds to the wave part of the solution, k, l and m are the components of the wave vector and ω is the frequency of the waves. The real part of the exponential balance the decrease of the density of the basic flow with height. The quantities with tilde denote the amplitudes of the solution.

By substituting the wave form in the linearised equations, we get a system of six linear equations for the solution amplitudes that can be written in the matrix form

$$\begin{pmatrix} -\mathrm{i}\hat{\omega} & -f & 0 & 0 & \mathrm{i}k & 0 \\ f & -\mathrm{i}\hat{\omega} & 0 & 0 & \mathrm{i}l & 0 \\ 0 & 0 & -\mathrm{i}\hat{\omega} & 0 & im - \frac{1}{2H} & g \\ 0 & 0 & \frac{N^2}{g} & -\mathrm{i}\hat{\omega} & 0 & 0 \\ \mathrm{i}k & \mathrm{i}l & im - \frac{1}{2H} & 0 & 0 & -\mathrm{i}\hat{\omega} \\ 0 & 0 & 0 & 1 & -\frac{1}{c_s^2} & 1 \end{pmatrix} \begin{pmatrix} \tilde{u} \\ \tilde{v} \\ \tilde{w} \\ \tilde{\theta} \\ \tilde{p} \\ \tilde{\rho} \end{pmatrix} = \begin{pmatrix} 0 \\ 0 \\ 0 \\ 0 \\ 0 \\ 0 \end{pmatrix}, \tag{1.26}$$

where $\hat{\omega} = \omega - \bar{u}k - \bar{v}l$ is the frequency of the waves observed in a reference frame that moves with the basic flow.

The system of equation has a non-trivial solution if and only if the determinant of the matrix is zero. This condition therefore provide us an equation relating the quantities contained in the matrix, which is the sought dispersion relation.

By evaluating the determinant of the matrix, we get

$$\begin{aligned} 0 = m\hat{\omega}\left(\hat{\omega}^2 - f^2\right)\left(\frac{g}{c_s^2} - \frac{1}{H} + \frac{N^2}{g}\right) + \mathrm{i}\hat{\omega}\Bigg[\frac{\hat{\omega}^2 - f^2}{2H}\left(\frac{g}{c_s^2} - \frac{1}{2H} + \frac{N^2}{g}\right) \\ -N^2(k^2+l^2) + \hat{\omega}^2\left(k^2+l^2+m^2\right) - \left(\hat{\omega}^2 - f^2\right)\frac{\hat{\omega}^2}{c_s^2} - m^2 f^2\Bigg]. \end{aligned} \tag{1.27}$$

The equality is satisfied if it holds for both the real and the imaginary part. To be able to divide the equation into these parts, we can multiply it by the complex conjugate of $\hat{\omega}$ and we divide the vertical wavevector component into the real and imaginary part $m = m_r + im_i$.

We assume that the wave does not propagate only horizontally, so it holds $m_r \neq 0$, and that $|\hat{\omega}| \neq |f|$, where the equality would correspond to a wave motion driven by the rotation of Earth rather than by the stratification. The real part of the equation is then satisfied if and only if it holds

$$\frac{g}{c_s^2} - \frac{1}{H} + \frac{N^2}{g} = 0. \tag{1.28}$$

This equality can be further used to simplify the relation given by the imaginary part of equation (1.27) to the form

$$\hat{\omega}^2\left(k^2+l^2+m^2+\frac{1}{4H^2} - \frac{\hat{\omega}^2 - f^2}{c_s^2}\right) = N^2\left(k^2+l^2\right) + f^2\left(m^2 + \frac{1}{4H^2}\right). \tag{1.29}$$

This relation still contains both the gravity waves and the sound waves. To get an equation just for the gravity waves, we make use of the fact that the speed of propagation of the sound waves is high and we take $c_s \to \infty$.

The limit step finally transforms the equation to the quadratic equation in $\hat{\omega}$,

$$\hat{\omega}^2 = \frac{N^2\left(k^2+l^2\right) + f^2\left(m^2 + \frac{1}{4H^2}\right)}{k^2+l^2+m^2+\frac{1}{4H^2}}, \tag{1.30}$$

that shows the relation of the frequency of the gravity waves to its wavevector components.

Moreover, after expressing the vertical wavenumber

$$m^2 = \frac{(N^2 - \hat{\omega}^2)\,(k^2 + l^2)}{\hat{\omega}^2 - f^2} - \frac{1}{4H^2}, \tag{1.31}$$

the relation indicates the bounds on the wave frequency: If the vertical component of the wave vector is real, then the left-hand side of equation (1.31) is positive. Consequently, the right-hand side of equation (1.31) also has to be positive. This can be ensured only if the signs of the terms $N^2 - \hat{\omega}^2$ and $\hat{\omega}^2 - f^2$ are the same, assuming that the horizontal wavevector components are also real. Because in the stably stratified atmosphere it usually holds that $f^2 < N^2$, the previous conditions on signs imply that $N^2 > \hat{\omega}^2 > f^2$. In other words, the frequency of the gravity waves cannot be larger than the Brunt-Väisälä frequency and smaller then the size of the Coriolis parameter.

The derivation of the dispersion relation was based on the assumption that the matrix in equation (1.26) is singular. This is equivalent to the statement that zero is an eigenvalue of the matrix. The dispersion relation can then be understood as a condition on the frequency $\hat{\omega}$, such that the matrix in equation (1.26) admits a zero eigenvalue.

For such $\hat{\omega}$, assuming the validity of the dispersion relation, it is possible to find at least one eigenvector corresponding to the zero eigenvalue of the matrix. These eigenvectors form a basis of the kernel of the matrix. By the description of the non-zero kernel, we can therefore find relations between the amplitudes of the solution $\tilde{u}$, $\tilde{v}$, $\tilde{w}$, $\tilde{\theta}$, $\tilde{p}$ and $\tilde{\rho}$. These relations, expressed in terms of the quantities that appear in the matrix equation (1.26), are called the polarization relations [6]. In particular, if the eigenvector is unique, the polarization relations connect pairs of the amplitude quantities.

The general evaluation of the kernel of the six by six matrix defined in (1.26) represents a tedious computation and it is not presented here. Instead, we only state the polarization relation connecting the amplitudes $\tilde{u}$ and $\tilde{w}$, which can be obtained by a few simple manipulations of the matrix. It reads

$$\tilde{w} = \left(\frac{\hat{\omega}^2 - f^2}{\hat{\omega}^2 - N^2}\right)\left(\frac{m + \frac{\mathrm{i}}{2H} - \mathrm{i}\,\frac{g}{c_s^2}}{\hat{\omega}k + \mathrm{i}fl}\right)\hat{\omega}\,\tilde{u}. \tag{1.32}$$

If we again assume the absence of sound waves by taking $c_s \to \infty$, the polarization relation for the gravity waves only can be simplified to

$$\tilde{w} = \left(\frac{\hat{\omega}^2 - f^2}{\hat{\omega}^2 - N^2}\right)\left(\frac{m + \frac{\mathrm{i}}{2H}}{\hat{\omega}k + \mathrm{i}fl}\right)\hat{\omega}\,\tilde{u}. \tag{1.33}$$

The polarization relation connecting the zonal and vertical velocity amplitudes (1.33) is of particular interest, as the product of the zonal and vertical velocity constitutes an important component of the momentum flux (see Section 2.2). Assuming that the frequency $\hat{\omega}$ is real, the factor before $\tilde{u}$ in (1.33) is not imaginary, unless $m = l = 0$ and k is real. Therefore, the real component of the product $\tilde{u}\tilde{w}$ in the momentum flux is generally zero only for strictly zonal waves or if one of the amplitudes $\tilde{u}$, $\tilde{w}$ is zero.

In the polarization relation (1.33), we can see that if k, l, m and $\hat{\omega}$ are all real and positive, the term in the second bracket has positive real part. Moreover, the

sign of the first bracket is always negative due to the derived relation $N^2 > \hat{\omega}^2 > f^2$. This implies that, under the assumptions above, the zonal velocity of GWs should have the opposite sign than the vertical velocity. The momentum flux component based on the product $\tilde{u}\tilde{w}$ is thus (in this approximation) negative.

Nevertheless, in the derivation, we used the linear theory only. In general, the dispersion relation and the polarization relations can be violated because of the dependence of the background flow on the wave activity.

2. Methodology

2.1 GW Detection Methods

In the context of this thesis, we want to study GW interactions and for this, GWs have to be identified in the data. The methods of separation of the gravity waves are mostly based on the linear perturbation theory – the data are divided into the small wave perturbations and the background. This is usually done by statistical methods such as fitting polynomials into the data [19] or by applying Fourier or Hilbert transform [20], [21]. Also, some more complex methods based on mode decomposition can be applied [22]. Finally, the gravity waves can be obtained from the data as deviations from some theoretical state of rest of the atmosphere [23]. In this chapter, we present some of the methods.

2.1.1 High-pass Filter Method

As a first separation method, we implement the high-pass filter method introduced in [20]. The method uses Gaussian filter, which modulates given fields of velocity components by convolution with a Gaussian function [24].

In the first step, a low pass filter is applied on the data to separate the GW related part. The frequencies of GWs to be filtered out are set by choosing a cutoff parameter L corresponding to the variance of the Gaussian function in the Fourier space. The gravity waves are subsequently obtained as a difference between the modulated and the original velocity fields.

In practice, the Fast Fourier transform (FFT) algorithm is used instead of convolution. To filter GWs from the data, FFT is first applied to the data. The Fourier coefficients are then multiplied by so-called response function

$$\hat{r}(k,l) = \mathrm{e}^{-\left(k^2+l^2\right)\frac{L^2}{4\pi^2}}, \tag{2.1}$$

where k and l are zonal and meridional wavenumbers, respectively. Finally, the inverse FFT algorithm is applied to the result of the multiplication.

The exponential function in formula (2.1) is, up to a scaling factor, a Gaussian function with variance σ^2 given by

$$\sigma^2 = \frac{2\pi^2}{L^2}. \tag{2.2}$$

As 95 % of the filtered waves will have wavenumber smaller then $2\sigma = 2\pi\sqrt{2}/L$, the wavelengths $\tilde{\lambda}$ that are filtered out fulfil

$$\tilde{\lambda} > \frac{L}{\sqrt{2}}. \tag{2.3}$$

After choosing an appropriate value to the parameter L, the waves with the wavelengths $\tilde{\lambda}$ that are filtered out by application of the response function (2.1) are commonly assumed to consist exclusively of GWs.

The complete procedure with subtraction of the filtered field from the initial one is equivalent to the filtering with response function

$$\hat{r}_{hp}(k,l) = 1 - \mathrm{e}^{-\left(k^2+l^2\right)\frac{L^2}{4\pi^2}}, \tag{2.4}$$

instead of (2.1). Therefore, we are effectively applying a high-pass filter method.

Before the FFT step, no periodization step is being applied, as the boundary effect is assumed to be small [20]. Instead, we only subtract global linear trend in the data. The periodization procedures will be discussed in Section 2.3.3.

2.1.2 Active Wind Method

The second method we present in more detail is a theory-based method introduced by Gassmann in article [25]. It divides the flow onto so-called active and inactive part. Unlike the standard GW separation methods, this method is not based on linear theory and can be used without any need for averaging and resulting wave mean separation.

In a coordinate system that rotates with the Earth, the equations of motion can be written in the form

$$\partial_t \mathbf{v} + (\mathbf{v} \cdot \nabla)\,\mathbf{v} = -\frac{1}{\rho}\nabla p - \nabla\phi - 2\boldsymbol{\Omega} \times \mathbf{v} + \mathbf{F}_r, \tag{2.5}$$

where $\mathbf{v}$ is the velocity, ρ is the density, p is the pressure. The gradient of geopotential $\nabla\phi$ describes the gravity force. The term $2\boldsymbol{\Omega}\times\mathbf{v}$ is the Coriolis force with angular velocity of the Earth $\boldsymbol{\Omega} = (0, \Omega\cos\varphi, \Omega\sin\varphi)$, where $\Omega = 1/24\ \mathrm{h}^{-1}$ and φ is the latitude. The force $\mathbf{F}_r$ is the frictional force. Further, we assume the validity of the state equation in the form for the ideal gas

$$\frac{p}{\rho} = R_d T. \tag{2.6}$$

The constant R_d is specific gas constant for dry air, $R_d = 287.04\,\mathrm{J\,kg^{-1}\,K^{-1}}$, and T is the temperature of the fluid.

We need to rewrite the equations of motion into a form more convenient for our study. To this end, we introduce several additional quantities. First, we define the Exner pressure Π,

$$\Pi = \left(\frac{p}{p_0}\right)^{R_d/c_p}. \tag{2.7}$$

Constant p_0 denotes reference pressure level $p_0 = 1000$ hPa, and c_p is specific heat at constant pressure for dry air, $c_p = 1004\,\mathrm{J\,kg^{-1}\,K^{-1}}$. The Exner pressure can further be expressed using potential temperature θ, which is defined as the temperature of a fluid parcel if it was adiabatically brought to the pressure level p_0. It holds

$$\Pi = \frac{T}{\theta}. \tag{2.8}$$

Using potential temperature, the thermodynamic equation supplementing the equations of motion takes the elegant form

$$\partial_t \theta + \mathbf{v} \cdot \nabla\theta = Q, \tag{2.9}$$

for diabatic heating Q.

Next, the Bernoulli function B, which represents the sum of kinetic, internal and potential energy of the fluid, is defined as

$$B = \frac{|\mathbf{v}|^2}{2} + c_p T + \phi. \tag{2.10}$$

Finally, we define the vector of absolute vorticity

$$\omega_a = 2\boldsymbol{\Omega} + \nabla \times \mathbf{v}. \tag{2.11}$$

To transform the equation (2.5), we first calculate the gradient of the Exner pressure

$$\nabla\Pi = \Pi\frac{R_d}{c_p}\frac{1}{p}\nabla p = \frac{1}{c_p}\frac{\Pi}{\rho T}\nabla p = \frac{1}{c_p}\frac{1}{\rho\theta}\nabla p, \tag{2.12}$$

where we used the definition of the Exner pressure (2.7), state equation (2.6) and formula (2.8).

Together with the vector calculus identity

$$\frac{1}{2}\nabla|\mathbf{v}|^2 = (\mathbf{v}\cdot\nabla)\,\mathbf{v} + \mathbf{v}\times(\nabla\times\mathbf{v}), \tag{2.13}$$

the gradient of the Exner pressure can be used to express the gradient of the Bernoulli function

$$\begin{aligned}\nabla B =& \nabla\frac{|\mathbf{v}|^2}{2} + c_p\nabla(\Pi\theta) + \nabla\phi \\ =& (\mathbf{v}\cdot\nabla)\,\mathbf{v} + \mathbf{v}\times(\nabla\times\mathbf{v}) + c_p\Pi\nabla\theta + \frac{1}{\rho}\nabla p + \nabla\phi \\ =& (\mathbf{v}\cdot\nabla)\,\mathbf{v} + \mathbf{v}\times\omega_a + 2\Omega\times\mathbf{v} + c_p\Pi\nabla\theta + \frac{1}{\rho}\nabla p + \nabla\phi.\end{aligned} \tag{2.14}$$

In the last equality, we used the definition of the absolute vorticity.

We rearrange equation (2.5) to

$$\begin{aligned}\partial_t\mathbf{v} = \Big(-(\mathbf{v}\cdot\nabla)\,\mathbf{v} - \mathbf{v}\times\omega_a - 2\boldsymbol{\Omega}\times\mathbf{v} - c_p\Pi\nabla\theta - \frac{1}{\rho}\nabla p - \nabla\phi\Big) \\ +\mathbf{v}\times\omega_a + c_p\Pi\nabla\theta + \mathbf{F}_r\end{aligned} \tag{2.15}$$

with the bracket equal to $-\nabla B$. Consequently, the governing equation (2.5) is equivalent to

$$\partial_t\mathbf{v} = -\nabla B + \mathbf{v}\times\omega_a + c_p\Pi\nabla\theta + \mathbf{F}_r, \tag{2.16}$$

which is the form we aimed at.

In the atmosphere, it is useful to describe the dynamical problems using the potential vorticity, as it interconnects the effects of rotation and stratification. Under certain conditions, the potential vorticity is conserved, which, together with the conservation of the Bernoulli function, enables the development of so-called Energy-Vorticity Theory [26].

This hydrodynamic theory has many advantages. One of them is the possibility to solve a system of non-linear differential equations for a general wind solution [27]

$$\mathbf{v} = \frac{\nabla\theta\times\nabla B}{\rho P} \tag{2.17}$$

analytically. The quantity P is the Ertel's potential vorticity defined as

$$P = \frac{1}{\rho}\omega_a\cdot\nabla\theta. \tag{2.18}$$

The solution (2.17) describes the part of the flow that streams along the intersection lines of planes with constant potential temperature and planes with constant Bernoulli function. The generality of the solution is based on the fact that it covers all the processes connected with both the energy and the potential vorticity conservation.

The balance (2.17) was used in [26] to introduce an index characterizing the dynamical state of the atmosphere, and subsequently in [25], the general wind solution was used for the definition of the inactive wind

$$\mathbf{v}_{ia} \equiv \frac{\nabla\theta \times \nabla B}{\rho P}, \tag{2.19}$$

which is a part of a flow that blows along the intersection lines as in the balanced case.

To further motivate the form of the inactive wind definition, we show a simple derivation of the balanced part of the flow. Since we try to find some kind of solution to a stationary flow, we need to be able to express the velocity from the governing equation with zero time derivative. For that reason, we take the cross product of equation (2.16) with $\nabla\theta$. After rearranging the terms, using the fact that $\nabla\theta \times \nabla\theta = 0$, this yields

$$\nabla\theta \times (\partial_t \mathbf{v} - \mathbf{F}_r) = -\nabla\theta \times \nabla B + \nabla\theta \times (\mathbf{v} \times \omega_a) \tag{2.20}$$

Using the vector identity $\mathbf{a} \times (\mathbf{b} \times \mathbf{c}) = \mathbf{b}\,(\mathbf{a} \cdot \mathbf{c}) - \mathbf{c}\,(\mathbf{a} \cdot \mathbf{b})$ and the prognostic equation for potential temperature (2.9), the second term on the right-hand side becomes

$$\begin{aligned} \nabla\theta \times (\mathbf{v} \times \omega_a) =& \mathbf{v}\,(\omega_a \cdot \nabla\theta) - \omega_a\,(\mathbf{v} \cdot \nabla\theta) \\ =& \mathbf{v}\,(\omega_a \cdot \nabla\theta) + \omega_a\,(\partial_t\theta - Q)\,. \end{aligned} \tag{2.21}$$

Therefore, we have

$$\nabla\theta \times (\partial_t \mathbf{v} - \mathbf{F}_r) - \omega_a\,(\partial_t\theta - Q) = -\nabla\theta \times \nabla B + \mathbf{v}\,(\omega_a \cdot \nabla\theta) \tag{2.22}$$

To simplify the notation, we use the definition of Ertel's potential vorticity. The last equation then reads

$$\nabla\theta \times (\partial_t \mathbf{v} - \mathbf{F}_r) - \omega_a\,(\partial_t\theta - Q) = -\nabla\theta \times \nabla B + \rho \mathbf{v} P. \tag{2.23}$$

The active wind method divides the flow into active and inactive part, where the inactive part describes stationary frictionless adiabatic flow. For the inactive flow, we therefore have $\partial_t \equiv 0$, $\mathbf{F}_r \equiv 0$ and $Q \equiv 0$, which implies that the left-hand side of equation (2.23) is zero. For the situations with $P \neq 0$, the inactive wind can be thus defined by equation (2.19).

The definition of the active wind does not provide us the solution to equation (2.23) with zero left-hand side, since the Bernoulli function B and Ertel's potential vorticity P still depend on the full velocity. On the other hand, it is justifiable thanks to the consistency with the Energy-Vorticity Theory.

The active wind corresponding to the perturbation to the balance flow is consequently defined as the complement of the inactive wind

$$\mathbf{v}_a \equiv \mathbf{v} - \mathbf{v}_{ia} = \mathbf{v} - \frac{\nabla\theta \times \nabla B}{\rho P}. \tag{2.24}$$

The active wind concept makes the wave effects on transport [25] and dynamics [23] explicit. Nevertheless, it include both the waves resulting from the rotation of Earth and the waves connected to stratification.

The separation of these two parts is in principle possible using the Helmholtz-Hodge decomposition. In the local domain, this is, however, complicated due to the assumption of the decomposition methods on the boundary conditions [28].

To be able to quantify the gravity wave activity using the active wind method, we apply procedure introduced in article [23] as a replacement of the Helmholtz-Hodge decomposition. The procedure utilizes the active wind velocity to evaluate the forcing in the equation of divergence and vorticity. We now present the procedure.

For the derivation of the forcing terms, we start by dividing the right-hand side of equation (2.16) on terms corresponding to the active wind and to the inactive wind,

$$\begin{aligned}
\partial_t \mathbf{v} =& -\nabla B + (\mathbf{v}_{ia} + \mathbf{v}_a) \times \omega_a + c_p \Pi \nabla\theta + \mathbf{F}_r \\
=& -\nabla B + \mathbf{v}_a \times \omega_a + \frac{\nabla\theta \times \nabla B}{\rho P} \times \omega_a + c_p \Pi \nabla\theta + \mathbf{F}_r \\
=& -\nabla B + \mathbf{v}_a \times \omega_a + \frac{\nabla B \left(\nabla\theta \cdot \omega_a\right) - \nabla\theta \left(\omega_a \cdot \nabla B\right)}{\rho P} + c_p \Pi \nabla\theta + \mathbf{F}_r \\
=& \mathbf{v}_a \times \omega_a + c_p \left(\Pi - \frac{\omega_a \cdot \nabla B}{c_p \rho P}\right) \nabla\theta + \mathbf{F}_r
\end{aligned} \tag{2.25}$$

where we used the definition of the inactive wind, the vector triple product identity and the definition of the Ertel's potential vorticity. After introducing a new quantity Π_a representing the Exner pressure for the active wind,

$$\Pi_a = \Pi - \frac{\omega_a \cdot \nabla B}{c_p \rho P}, \tag{2.26}$$

the previous equation can be written as

$$\partial_t \mathbf{v} = \mathbf{v}_a \times \omega_a + c_p \Pi_a \nabla\theta + \mathbf{F}_r. \tag{2.27}$$

We further rearrange equation (2.27) by eliminating the active wind Exner pressure Π_a, so that the equation can be transformed to the equations of horizontal divergence and vertical vorticity, in which we could evaluate the forcing.

For the next computations, we use the z-coordinate system. We denote the components of the absolute vorticty by ω_x, ω_y and ω_z, the components of velocity u, v, w and the components of the frictional force $F_{r,x}$, $F_{r,y}$ and $F_{r,z}$. The subscript a after a velocity component again refers to the active wind part of the flow.

The z component of equation (2.27)

$$\partial_t w = -\omega_x v_a + \omega_y u_a + c_p \Pi_a \partial_z \theta + F_{r,z} \tag{2.28}$$

can be used to eliminate the Exner pressure in (2.27). We have

$$\partial_t \mathbf{v} = -\omega_a \times \mathbf{v}_a + \frac{\nabla\theta}{\partial_z \theta} \left(\partial_t w + \omega_x v_a - \omega_y u_a - F_{r,z}\right) + \mathbf{F}_r. \tag{2.29}$$

When we introduce the horizontal velocity vector $\mathbf{v}_h = (u, v, 0)$, horizontal friction force $\mathbf{F}_{r,h} = (F_{r,x}, F_{r,y}, 0)$ and the horizontal gradient $\nabla_h = (\partial_x, \partial_y, 0)$, the previous equation is equivalent to

$$\partial_t \mathbf{v}_h - \frac{\nabla_h \theta}{\partial_z \theta} \partial_t w = -\omega_a \times \mathbf{v}_a + \frac{\nabla \theta}{\partial_z \theta} \left(\omega_x v_a - \omega_y u_a\right) + \mathbf{F}_{r,h} - \frac{\nabla_h \theta}{\partial_z \theta} F_{r,z}. \tag{2.30}$$

Now, we focus on the first two terms on the right-hand side of equation (2.30). Using the component notation, they can be rearranged as follows,

$$\begin{aligned} -\omega_a \times \mathbf{v}_a + & \frac{\nabla \theta}{\partial_z \theta} \left(\omega_x v_a - \omega_y u_a\right) \\ &= \begin{pmatrix} -\omega_y w_a + \omega_z v_a + \frac{\partial_x \theta}{\partial_z \theta} \left(\omega_x v_a - \omega_y u_a\right) \\ -\omega_z u_a + \omega_x w_a + \frac{\partial_y \theta}{\partial_z \theta} \left(\omega_x v_a - \omega_y u_a\right) \\ -\omega_x v_a + \omega_y u_a + \left(\omega_x v_a - \omega_y u_a\right) \end{pmatrix} \\ &= \begin{pmatrix} -\omega_y \left(w_a + \frac{\partial_x \theta}{\partial_z \theta} u_a + \frac{\partial_y \theta}{\partial_z \theta} v_a\right) + v_a \left(\omega_z + \frac{\partial_x \theta}{\partial_z \theta} \omega_x + \frac{\partial_y \theta}{\partial_z \theta} \omega_y\right) \\ +\omega_x \left(w_a + \frac{\partial_x \theta}{\partial_z \theta} u_a + \frac{\partial_y \theta}{\partial_z \theta} v_a\right) - u_a \left(\omega_z + \frac{\partial_x \theta}{\partial_z \theta} \omega_x + \frac{\partial_y \theta}{\partial_z \theta} \omega_y\right) \\ 0 \end{pmatrix} \\ &= w^* \left(\mathbf{k} \times \omega_h\right) - \zeta_a^* \left(\mathbf{k} \times \mathbf{v}_{a,h}\right). \end{aligned} \tag{2.31}$$

In the last equality, we introduced the vector of horizontal absolute vorticity $\omega_h = (\omega_x, \omega_y, 0)$, the vector of horizontal active wind velocity $\mathbf{v}_{a,h} = (u_a, v_a, 0)$, the unit vector in the z-direction $\mathbf{k} = (0, 0, 1)$ and quantities w^* and ζ_a^*. The quantity w^* represents the vertical velocity of the wind that blows along isentropes and it is defined by formula

$$w^* = \frac{\mathbf{v}_a \cdot \nabla \theta}{\partial_z \theta}. \tag{2.32}$$

Similarly, the quantity ζ_a^* is related to the absolute vorticity by the formula

$$\zeta_a^* = \frac{\omega_a \cdot \nabla \theta}{\partial_z \theta}. \tag{2.33}$$

We can therefore rewrite equation (2.30) to

$$\partial_t \mathbf{v}_h - \frac{\nabla_h \theta}{\partial_z \theta} \partial_t w = w^* \left(\mathbf{k} \times \omega_h\right) - \zeta_a^* \left(\mathbf{k} \times \mathbf{v}_{a,h}\right) + \mathbf{F}_{r,h} - \frac{\nabla_h \theta}{\partial_z \theta} F_{r,z}. \tag{2.34}$$

To simplify the notation, we further introduce the vectors

$$\mathbf{g}_1 = \mathbf{v}_{a,h} \zeta_a^*, \qquad \mathbf{g}_2 = -w^* \omega_h. \tag{2.35}$$

The vector $\mathbf{g}_1$ characterizes the motions connected with the horizontal advection of vorticity, the vector $\mathbf{g}_2$ describes rather the vertical advection of vorticity. Using these definitions, we can reformulate the previous equation for velocity evolution to

$$\partial_t \mathbf{v}_h - \frac{\nabla_h \theta}{\partial_z \theta} \partial_t w = -\mathbf{k} \times \left(\mathbf{g}_1 + \mathbf{g}_2\right) + \mathbf{F}_{r,h} - \frac{\nabla_h \theta}{\partial_z \theta} F_{r,z}. \tag{2.36}$$

Finally, by applying the horizontal divergence operator $\nabla_h \cdot$ to the equation (2.36), it is possible to get the equation for evolution of the horizontal divergence $\delta = \partial_x u + \partial_y v$,

$$\partial_t \delta = -\nabla_h \cdot \left(\mathbf{k} \times \left(\mathbf{g}_1 + \mathbf{g}_2\right)\right) + \nabla_h \cdot \mathbf{F}_{r,h} + \nabla_h \cdot \left(\frac{\nabla_h \theta}{\partial_z \theta} \left(\partial_t w - F_{r,z}\right)\right). \tag{2.37}$$

Because the vector $\mathbf{k}$ is constant and its only non-zero component is the z-component, the first term on the right-hand side can be reformulated. We get the equation

$$\partial_t \delta = \mathbf{k} \cdot \nabla \times (\mathbf{g}_1 + \mathbf{g}_2) + \nabla_h \cdot \mathbf{F}_{r,h} + \nabla_h \cdot \left(\frac{\nabla_h \theta}{\partial_z \theta} \left(\partial_t w - F_{r,z} \right) \right). \tag{2.38}$$

Similarly, we apply the z-component of the curl operator to equation (2.36) to obtain the equation for the vertical component ζ of the vorticity vector,

$$\partial_t \zeta = \mathbf{k} \cdot \nabla \times [\mathbf{k} \times (\mathbf{g}_1 + \mathbf{g}_2)] + \mathbf{k} \cdot \nabla \times \mathbf{F}_{r,h} + \mathbf{k} \cdot \nabla \times \left(\frac{\nabla_h \theta}{\partial_z \theta} \left(\partial_t w - F_{r,z} \right) \right). \tag{2.39}$$

Using the fact that the vectors $\mathbf{g}_1$ and $\mathbf{g}_2$ are already horizontal and that $\mathbf{k}$ is a constant vector, this is equivalent to the equation

$$\partial_t \zeta = \nabla \cdot (\mathbf{g}_1 + \mathbf{g}_2) + \mathbf{k} \cdot \nabla \times \mathbf{F}_{r,h} + \mathbf{k} \cdot \nabla \times \left(\frac{\nabla_h \theta}{\partial_z \theta} \left(\partial_t w - F_{r,z} \right) \right). \tag{2.40}$$

As proposed in article [23], we now consider only terms in equations (2.38) and (2.40) that are not related to the dissipation. Also, we do not consider the term containing the time derivative of the vertical velocity. Then the evolution of divergence and vorticity driven by the non-dissipative forces only can be written as

$$\partial_t \delta = \mathbf{k} \cdot \nabla \times (\mathbf{g}_1 + \mathbf{g}_2), \tag{2.41a}$$

$$\partial_t \zeta = \nabla \cdot (\mathbf{g}_1 + \mathbf{g}_2). \tag{2.41b}$$

By evaluating the vector $\mathbf{g} = \mathbf{g}_1 + \mathbf{g}_2$, we can get the forcing to the equations.

In particular, by this procedure, the right-hand side of the divergence equation describes the gravity wave dynamics only, as the curl applied to the vector $\mathbf{g}$ filters out the rotational part of the vector. The assumption on the non-linear balance defined by (2.19) successfully removes the terms related to the balance from the divergence equation.

2.1.3 Other GW Separation Methods

Another theoretical method for GW separation is the method based on the omega equation described in article [29]. The omega equation is an equation describing vertical motion in the pressure coordinate system on a sphere. The separation method considers the second-order asymptotic expansion of the balanced vertical velocity in Rossby number. Basically, the omega equation is divided into parts corresponding to different powers of the Rossby number and numerically solved for the components of the balanced vertical velocity corresponding to the same powers. The wave perturbations of the vertical velocity are obtained as a difference between the balanced and original flow. The method was introduced for global model but nothing seems to prevent its utilization in regional domains.

A separation method developed by using a completely different principle is the multi-dimensional ensemble empirical mode decomposition method introduced in article [22]. The method fundamentally divides the data into different modes by

repetitively computing the minimal and maximal envelopes and subtracting them from the data. It is similar to the decomposition into Fourier series but the basis functions are not a priori given but they are found by the computations. The advantage of this method is that it can, unlike methods that use Fourier transform, describe well even very localized effects. For the space and time limitations we let those two diagnostics for future work.

Further, there are other GW separation methods that are suitable only for a global domain. For instance, the method described in article [30] decomposes the data into Fourier series with Hough harmonics as the basis functions. Hough harmonics are a natural choice of basis functions as they are eigenfunctions of the general se of equations on a sphere for an unforced atmosphere [31].

Besides the theoretical methods, there exist several statistical approaches for GW separations [21], [32], [33]. They rely on various assumptions, typically on monochromaticity.

2.2 GW Momentum Fluxes and Drag

As the wind blows against a mountainside, it exerts pressure force on the mountain surface. In accordance with Newton's third law, this gives rise to a drag force acting in the opposite direction on the air, which is called a mountain drag. The mountain drag is deposited not only locally in the vicinity of the mountain, but is also propagated by the mountain waves (alternatively called lee waves, a special type of GWs) to the free atmosphere, where the mountain wave drag (MWD) is deposited at the level of their dissipation. Hence, the mountain waves get the momentum flux (MF) and propagate it further in the atmosphere [34]. Estimating the drag exerted by freely propagating GWs is a complex task for which various methodologies exist. Below we detail a method based on linear theory and spatial averaging.

We start by considering compressible inviscid flow on a rotating sphere. Using the standard scale-analysis argumentation [17], it is possible to write governing equation for the horizontal velocity components in the corotating coordinate system in the form

$$\partial_t u + u\partial_x u + v\partial_y u + w\partial_z u = -\frac{1}{\rho}\partial_x p + fv \tag{2.42a}$$

$$\partial_t v + u\partial_x v + v\partial_y v + w\partial_z v = -\frac{1}{\rho}\partial_y p - fu, \tag{2.42b}$$

where u, v and w are zonal, meridional and vertical wind components, p is the pressure and f is the Coriolis parameter.

We apply a linear perturbation method, assuming that the velocity components can be decomposed into a slowly varying mean flow and a small perturbation corresponding to the wave motion,

$$u = \langle u \rangle + u', \tag{2.43a}$$

$$v = \langle v \rangle + v', \tag{2.43b}$$

$$w = w', \tag{2.43c}$$

where the mean vertical velocity component is taken zero. We further assume that the density is a function of altitude only. In computations, this is achieved by taking integral mean value of density $\hat{\rho}(z)$ over respective levels.

Next, we demonstrate the derivation for zonal momentum equation (2.42a) only, the steps for the meridional component are analogous. With use of the continuity equation

$$\partial_t \rho + \partial_x(\rho u) + \partial_y(\rho v) + \partial_z(\rho w) = 0, \tag{2.44}$$

it is possible to pass from (2.42a) to the equation in the flux form

$$\partial_t(\rho u) + \partial_x(\rho u^2) + \partial_y(\rho uv) + \partial_z(\rho uw) = -\partial_x p + fv \tag{2.45}$$

Substituting the decomposition (2.43) and the assumption on density, we get

$$\begin{aligned} \partial_t(\langle u\rangle + u') + \partial_x\left(\left(\langle u\rangle + u'\right)^2\right) + \partial_y\left(\left(\langle u\rangle + u'\right)\left(\langle v\rangle + v'\right)\right) \\ + \frac{1}{\hat{\rho}}\partial_z\left(\hat{\rho}\left(\langle u\rangle + u'\right)w'\right) \\ = -\frac{1}{\hat{\rho}}\partial_x p + f\left(\langle v\rangle + v'\right) \end{aligned} \tag{2.46}$$

At this stage, we average (2.46) over area A of the selected horizontal domain, which will be denoted by line over the quantities.

The selected domain should not be too small, so that we can assume that $\overline{u'} = 0$. Otherwise, we might capture more ridges or troughs of some distinct waves and the assumption would be violated. On the other hand, we need to assume that $\overline{\langle\cdot\rangle\,(\cdot)'} = 0$, which is possible only if the domain is not too broad and so the mean flow variables $\langle\cdot\rangle$ do not change much.

With the assumption that the perturbations of velocity components have zero average over the domain at every altitude and that the velocity field is such that the interchange of derivative and integral is possible, the first term is averaged to

$$\overline{\partial_t(\langle u\rangle + u')} = \partial_t\overline{\langle u\rangle} \tag{2.47}$$

Using the fundamental theorem of calculus, the averages of the second and the third term in (2.46) are

$$\overline{\partial_x\left(\left(\langle u\rangle + u'\right)^2\right)} = \frac{1}{A}\left[\int\left(\langle u\rangle + u'\right)^2 \mathrm{d}y\right]_{x_1}^{x_2}, \tag{2.48}$$

$$\overline{\partial_y\left(\left(\langle u\rangle + u'\right)\left(\langle v\rangle + v'\right)\right)} = \frac{1}{A}\left[\int\left(\langle u\rangle + u'\right)\left(\langle v\rangle + v'\right)\mathrm{d}x\right]_{y_1}^{y_2}. \tag{2.49}$$

For the last integral on the left-hand side of (2.46), we have

$$\frac{1}{\hat{\rho}}\overline{\partial_z\left(\hat{\rho}\left(\langle u\rangle + u'\right)w'\right)} = \frac{1}{A}\frac{1}{\hat{\rho}}\partial_z\iint\hat{\rho}\left(\langle u\rangle + u'\right)w'\,\mathrm{d}x\,\mathrm{d}y \tag{2.50}$$

If we further consider the average of $\langle\cdot\rangle\,(\cdot)'$ over faces to be zero, the previous three averaged terms can be thus simplified to

$$\overline{\partial_x\left(\left(\langle u\rangle + u'\right)^2\right)} = \frac{1}{A}\left[\int\left(\langle u\rangle^2 + \left(u'\right)^2\right)\mathrm{d}y\right]_{x_1}^{x_2}, \tag{2.51}$$

$$\overline{\partial_y \left(\left(\langle u \rangle + u' \right) \left(\langle v \rangle + v' \right) \right)} = \frac{1}{A} \left[\int \left(\langle u \rangle \langle v \rangle + u'v' \right) \mathrm{d}x \right]_{y_1}^{y_2}, \tag{2.52}$$

$$\frac{1}{\hat{\rho}} \overline{\partial_z \left(\hat{\rho} \left(\langle u \rangle + u' \right) w' \right)} = \frac{1}{A} \frac{1}{\hat{\rho}} \partial_z \iint \hat{\rho} u'w' \, \mathrm{d}x \, \mathrm{d}y. \tag{2.53}$$

To deal with the right-hand size of equation (2.46), we write the velocity as a sum of velocities of geostrophic and ageostrophic flow, $u = u_g + u_a$, $v = v_g + v_a$. Geostrophic flow is an idealized stationary flow described by the balance of pressure and Coriolis force, considering advective terms to be negligible. From equations (2.42), we have

$$u_g = -\frac{\partial_y p}{\rho f}, \quad v_g = \frac{\partial_x p}{\rho f}. \tag{2.54}$$

Therefore, averaged right-hand side of equation (2.46) can be written as

$$\overline{-\frac{1}{\hat{\rho}} \partial_x p + f \left(\langle v \rangle + v' \right)} = \overline{-f v_g + f v} = \overline{f v_a}. \tag{2.55}$$

Altogether, the averaged equation (2.46) has the form

$$\begin{aligned} \partial_t \langle u \rangle = & - \frac{1}{A} \left[\int \left(\langle u \rangle^2 + \left(u' \right)^2 \right) \mathrm{d}y \right]_{x_1}^{x_2} \\ & - \frac{1}{A} \left[\int \left(\langle u \rangle \langle v \rangle + u'v' \right) \mathrm{d}x \right]_{y_1}^{y_2} \\ & - \frac{1}{A} \frac{1}{\hat{\rho}} \partial_z \iint \hat{\rho} u'w' \, \mathrm{d}x \, \mathrm{d}y + \overline{f v_a}. \end{aligned} \tag{2.56}$$

The terms on the right-hand side can be divided into terms corresponding to the wave motion and terms corresponding to motions on larger scale. In particular, it is possible to identify three terms that add up to the zonal component of MWD,

$$MWD_{xx} = -\frac{1}{A} \left[\int \left(u' \right)^2 \mathrm{d}y \right]_{x_1}^{x_2}, \tag{2.57a}$$

$$MWD_{yx} = -\frac{1}{A} \left[\int u'v' \, \mathrm{d}x \right]_{y_1}^{y_2}, \tag{2.57b}$$

$$MWD_{zx} = -\frac{1}{A} \frac{1}{\hat{\rho}} \partial_z \iint \hat{\rho} u'w' \, \mathrm{d}x \, \mathrm{d}y. \tag{2.57c}$$

The quantity MWD_{xx} is zonal derivative of zonal flux of zonal wave momentum, MWD_{yx} is meridional derivative of meridional flux of zonal wave momentum and MWD_{zx} is vertical derivative of vertical flux of zonal wave momentum.

Analogously, for the meridional velocity component, it is possible to get equation

$$\begin{aligned} \partial_t \langle v \rangle = & - \frac{1}{A} \left[\int \left(\langle u \rangle \langle v \rangle + u'v' \right) \mathrm{d}y \right]_{x_1}^{x_2} \\ & - \frac{1}{A} \left[\int \left(\langle v \rangle^2 + \left(v' \right)^2 \right) \mathrm{d}x \right]_{y_1}^{y_2} \\ & - \frac{1}{A} \frac{1}{\hat{\rho}} \partial_z \iint \hat{\rho} v'w' \, \mathrm{d}x \, \mathrm{d}y - \overline{f u_a}. \end{aligned} \tag{2.58}$$

We get terms of the meridional component of MWD,

$$MWD_{xy} = -\frac{1}{A}\left[\int u'v' \,\mathrm{d}y\right]_{x_1}^{x_2}, \tag{2.59a}$$

$$MWD_{yy} = -\frac{1}{A}\left[\int (v')^2 \,\mathrm{d}x\right]_{y_1}^{y_2}, \tag{2.59b}$$

$$MWD_{zy} = -\frac{1}{A}\frac{1}{\hat{\rho}}\partial_z \iint \hat{\rho} v'w' \,\mathrm{d}x\,\mathrm{d}y. \tag{2.59c}$$

However, we only got results in the local Cartesian system. To be able to compute MWD in larger domains, we need to use spherical coordinates. In that case, it is necessary to proceed more carefully in steps using fundamental theorem of calculus, such as (2.48). We illustrate it on examples of MWD_{xx} and MWD_{yx}, modifying slightly their definition.

We denote the Earth radius by r_e, radial coordinate by r, latitude by φ and longitude by λ. Assuming that altitudes of the domain are much smaller than the radius of Earth, we have

$$\begin{aligned} MWD_{xx} &= -\frac{1}{A}\iint \partial_x\left(u'^2\right) r^2 \cos\varphi \,\mathrm{d}\lambda\,\mathrm{d}\varphi \\ &= -\frac{r^2}{A}\iint \partial_\lambda\left(u'^2\right)(\partial_x\lambda)\cos\varphi \,\mathrm{d}\lambda\,\mathrm{d}\varphi \\ &= -\frac{r}{A}\iint \partial_\lambda\left(u'^2\right)\mathrm{d}\lambda\,\mathrm{d}\varphi \approx -\frac{r_e}{A}\left[\int u'^2 \,\mathrm{d}\varphi\right]_{\lambda_1}^{\lambda_2}, \end{aligned} \tag{2.60}$$

where the area A bounded by latitudes φ_1 and φ_2 and longitudes λ_1 and λ_2 is given by

$$A = \iint r^2 \cos\varphi \,\mathrm{d}\lambda\,\mathrm{d}\varphi \approx r_e^2\left(\lambda_2 - \lambda_1\right)\left(\sin\varphi_1 - \sin\varphi_2\right). \tag{2.61}$$

For MWD_{yx}, the integration by parts is needed. It holds

$$\begin{aligned} MWD_{yx} &= -\frac{1}{A}\iint \partial_y\left(u'v'\right) r^2 \cos\varphi \,\mathrm{d}\lambda\,\mathrm{d}\varphi \\ &= -\frac{r^2}{A}\iint \partial_\varphi\left(u'v'\right)(\partial_y\varphi)\cos\varphi \,\mathrm{d}\lambda\,\mathrm{d}\varphi \\ &= -\frac{r}{A}\iint \partial_\varphi\left(u'v'\right)\cos\varphi \,\mathrm{d}\lambda\,\mathrm{d}\varphi \\ &\approx -\frac{r_e}{A}\left[\int u'v'\cos\varphi \,\mathrm{d}\lambda\right]_{\varphi_1}^{\varphi_2} - \frac{r_e}{A}\iint u'v'\sin\varphi \,\mathrm{d}\lambda\,\mathrm{d}\varphi. \end{aligned} \tag{2.62}$$

In the same way, one can get

$$MWD_{yy} \approx -\frac{r_e}{A}\left[\int v'^2\cos\varphi \,\mathrm{d}\lambda\right]_{\varphi_1}^{\varphi_2} - \frac{r_e}{A}\iint v'^2\sin\varphi \,\mathrm{d}\lambda\,\mathrm{d}\varphi, \tag{2.63}$$

$$MWD_{xy} \approx -\frac{r_e}{A}\left[\int u'v' \,\mathrm{d}\varphi\right]_{\lambda_1}^{\lambda_2}, \tag{2.64}$$

$$MWD_{zx} \approx -\frac{r_e^2}{A}\frac{1}{\hat{\rho}}\partial_r \iint \hat{\rho} u'w' \cos\varphi \,\mathrm{d}\lambda\,\mathrm{d}\varphi - \frac{2r_e}{A}\frac{1}{\hat{\rho}}\iint \hat{\rho} u'w' \cos\phi \,\mathrm{d}\lambda\,\mathrm{d}\phi, \tag{2.65}$$

$$MWD_{zy} \approx -\frac{r_e^2}{A}\frac{1}{\hat{\rho}}\partial_r \iint \hat{\rho} v' w' \cos\varphi \,\mathrm{d}\lambda \,\mathrm{d}\varphi - \frac{2r_e}{A}\frac{1}{\hat{\rho}} \iint \hat{\rho} v' w' \cos\phi \,\mathrm{d}\lambda \,\mathrm{d}\phi. \quad (2.66)$$

Also, we consider the vertical fluxes of zonal and meridional momentum

$$MF_{zx} \approx \frac{r_e^2}{A} \iint \hat{\rho} u' w' \cos\varphi \,\mathrm{d}\lambda \,\mathrm{d}\varphi, \quad (2.67)$$

$$MF_{zy} \approx \frac{r_e^2}{A} \iint \hat{\rho} v' w' \cos\varphi \,\mathrm{d}\lambda \,\mathrm{d}\varphi. \quad (2.68)$$

The considered approximation $r_e \approx r$ is well justifiable, since the altitudes in the troposphere and stratosphere are about 1000 times smaller than the Earth radius. By the substitution of r for r_e and the substitution of r^2 for r_e^2, we thus make an error in the third or in the sixth digit, respectively. The approximation in the factor $1/A$ is also reasonable, since, in view of equation (2.61), for a constant c it holds

$$\frac{1}{A} = cr^{-2} = c\,(r_e + z)^{-2} \approx c\,(r_e - 2z) \quad (2.69)$$

by the Taylor expansion.

2.3 Effective Resolution and GW Spectra

2.3.1 Horizontal Energy Spectrum

In this section, we describe the methods of computation of the horizontal spectrum of specific kinetic energy at a given altitude.

Total kinetic energy at an altitude z with a unitary density is given by formula

$$E^z = \frac{1}{2}\int\int \left(u^2(x,y,z) + v^2(x,y,z)\right) \mathrm{d}x \,\mathrm{d}y \quad (2.70)$$

$$\approx \frac{1}{2}\sum_{i=0}^{N-1}\sum_{j=0}^{N-1} \left(u_{i,j}^2 + v_{i,j}^2\right)(\Delta x)^2, \quad (2.71)$$

where $u_{i,j} = u(x_i, y_j)$ and $v_{i,j} = v(x_i, y_j)$ are the components of velocity at individual grid points, N denotes number of grid point in each direction and Δx is the horizontal distance between grid points.

To get the spectrum, it is convenient to describe the energy in the Fourier space. We use the definition of the two-dimensional discrete Fourier transform (DFT)

$$\hat{a}_{k,l} = \sum_{n=0}^{N-1}\sum_{m=0}^{N-1} a_{n,m} \mathrm{e}^{-2\pi\mathrm{i}\frac{nk}{N}} \mathrm{e}^{-2\pi\mathrm{i}\frac{ml}{N}}, \quad k,l = 0,\ldots,N-1, \quad (2.72)$$

with its inverse

$$a_{m,n} = \frac{1}{N^2}\sum_{k=0}^{N-1}\sum_{l=0}^{N-1} \hat{a}_{k,l} \mathrm{e}^{2\pi\mathrm{i}\frac{nk}{N}} \mathrm{e}^{2\pi\mathrm{i}\frac{ml}{N}}, \quad m,n = 0,\ldots,N-1. \quad (2.73)$$

By the Parseval theorem for two-dimensional DFT given by equation (2.72) [35], it holds

$$\sum_{i=0}^{N-1}\sum_{j=0}^{N-1}\left(u_{i,j}^2+v_{i,j}^2\right)=\frac{1}{N^2}\sum_{k=0}^{N-1}\sum_{l=0}^{N-1}\left(\hat{u}_{k,l}\hat{u}_{k,l}^*+\hat{v}_{k,l}\hat{v}_{k,l}^*\right) \tag{2.74}$$

with $\hat{u}_{k,l}$ and $\hat{v}_{k,l}$ obtained by the DFT of velocity components. The symbol $*$ denotes the complex conjugate. The latter expression can already be used to compute specific kinetic energy for individual numbers k and l as

$$E_{k,l}^z=\frac{1}{2N^2}\left(\hat{u}_{k,l}\hat{u}_{k,l}^*+\hat{v}_{k,l}\hat{v}_{k,l}^*\right). \tag{2.75}$$

In the atmosphere, it is useful to decompose the energy into the vortical and divergent part to distinguish between waves governed by the two dominant mechanisms, rotation and stratification.

The vorticity ζ and divergence δ at given altitude z at a grid point i,j is defined as

$$\zeta_{i,j}^z=\zeta(x_i,y_j,z)=\left(\frac{\partial v(x',y',z')}{\partial x}-\frac{\partial u(x',y',z')}{\partial y}\right)\Bigg|_{(x',y',z')=(x_i,y_j,z)}, \tag{2.76}$$

$$\delta_{i,j}^z=\delta(x_i,y_j,z)=\left(\frac{\partial u(x',y',z')}{\partial x}+\frac{\partial v(x',y',z')}{\partial y}\right)\Bigg|_{(x',y',z')=(x_i,y_j,z)}. \tag{2.77}$$

By the analogy with continuous Fourier transform with the same scaling as in equation (2.72), realizing that $x_m\sim m\Delta x$, these formulas can be transformed to

$$\hat{\zeta}_{k,l}^z=\frac{2\pi\mathrm{i}}{N\Delta x}\left(k\hat{v}_{k,l}-l\hat{u}_{k,l}\right), \tag{2.78}$$

$$\hat{\delta}_{k,l}^z=\frac{2\pi\mathrm{i}}{N\Delta x}\left(k\hat{u}_{k,l}+l\hat{v}_{k,l}\right). \tag{2.79}$$

These equations imply that

$$\hat{\zeta}_{k,l}^z(\hat{\zeta}_{k,l}^z)^*+\hat{\delta}_{k,l}^z(\hat{\delta}_{k,l}^z)^*=\left(\frac{2\pi}{N\Delta x}\right)^2\left(k^2+l^2\right)\left(\hat{u}_{k,l}\hat{u}_{k,l}^*+\hat{v}_{k,l}\hat{v}_{k,l}^*\right) \tag{2.80}$$

Therefore, formula (2.75) for the specific horizontal kinetic energy can be rewritten to the final form

$$E_{k,l}^z=\frac{1}{2N^2}\frac{\hat{\zeta}_{k,l}^z(\hat{\zeta}_{k,l}^z)^*+\hat{\delta}_{k,l}^z(\hat{\delta}_{k,l}^z)^*}{\left(\frac{2\pi}{N\Delta x}\right)^2\left(k^2+l^2\right)} \tag{2.81}$$

for $k,l=0,\ldots,N-1$. The term in the denominator

$$K^2\equiv\left(\frac{2\pi}{N\Delta x}\right)^2\left(k^2+l^2\right) \tag{2.82}$$

represent the square of the size of horizontal wave vector corresponding to the horizontal wavelength $\lambda=2\pi/K$.

As we need the spectrum with respect to the horizontal wavelength, we sum up the values $E^z_{k,l}$ of specific energy with similar values of K [36]. More precisely, we consider the sequence of wavenumbers

$$K_n = \frac{2\pi}{N\Delta x} n, \quad n = 1, 2, \ldots, \left[\frac{N}{2}\right] - 1 \tag{2.83}$$

with the upper bound corresponding to the Nyquist frequency. We further denote

$$\Delta K = \frac{2\pi}{N\Delta x} \tag{2.84}$$

the difference between two consecutive wavenumbers of this sequence. The specific horizontal kinetic energy for the wavenumbers in the sequence can then be computed by the formula

$$E^z(K_n) = \sum_{|(k,l)| \in I_n} E^z_{k,l}, \tag{2.85}$$

where $I_n = (K_n - \Delta K/2, K_n + \Delta K/2)$ is an interval around K_n.

By the theory, it is possible to expect that the horizontal kinetic energy spectrum is proportional to $K^{-5/3}$ for smaller scales and it is proportional to K^{-3} for larger scales [37],[38]. The former dependence is known as the Kolmogorov spectrum. It follows from the assumption that the energy spectrum depends on the dissipation of the energy. The latter dependence, based on the quasi two-dimensional theory of turbulence at large scales, is related to the vorticity. Such theoretical proportionates were repeatedly confirmed by the studies of high-resolution simulations [36],[39] or by processing of aircraft measurement [40],[41].

2.3.2 Vertical Energy Spectrum

More information about the gravity waves in the model can be obtained by studying the vertical spectrum of the potential energy. In this subsection, we describe the formula we use for the potential energy.

An illustrative derivation of the formula can be performed using a fluid parcel reasoning [6]. At an arbitrary altitude, we set the vertical coordinate z to zero, and we denote the density at the level by ρ_0. Since the pressure generally decreases with altitude, we assume that the density near the level $z = 0$ can be approximated by $\bar{\rho} \approx \rho_0 (1 - z/H)$, where H is a constant value characterizing the density profile at the altitude $z = 0$. This corresponds to the fact that the Brunt-Väisälä frequency N_0 defined by the formula (1.5) is around the level approximately constant, $N_0^2 = g/H$.

In this setting, the potential energy can be calculated by considering the energy needed for the exchange of two fluid parcels that are located at levels $z = -\delta$ and $z = \delta$. When the particles are in their original positions, the potential energy with respect to the level $z = 0$ for the two parcels is

$$E_1 = g\rho_0 \left(1 + \frac{\delta}{H}\right)(-\delta) + g\rho_0 \left(1 - \frac{\delta}{H}\right)\delta, \tag{2.86}$$

where we applied the standard formula for the potential energy computation with the considered density profile. After the exchange of the two parcels, their total

potential energy is

$$E_2 = g\rho_0 \left(1 - \frac{\delta}{H}\right)(-\delta) + g\rho_0 \left(1 + \frac{\delta}{H}\right)\delta. \tag{2.87}$$

For the energy difference, we can write

$$\Delta E = E_2 - E_1 = 4\rho_0 \delta^2 \frac{g}{H}. \tag{2.88}$$

To get the energy associated with just one of the parcels, we take $\Delta E/2$. To rewrite the formula for the definition of potential energy in more general situation, we further denote the fraction g/H by N_0^2 and the total vertical displacement 2δ by ξ. Subsequently, the potential energy can be defined as

$$E_p = \frac{1}{2}\rho_0 N_0^2 \xi^2. \tag{2.89}$$

To be able to evaluate the formula, it is necessary to rewrite the displacement ξ into a more convenient form. This can be done by the assumption that for a small displacement, the total displacement corresponds to the fluctuation of density ρ'. More precisely, we can write

$$\rho' = -\frac{\mathrm{d}\bar{\rho}}{\mathrm{d}z}\xi \approx \frac{\rho_0}{H}\xi, \tag{2.90}$$

which is the approximation by Taylor polynomial for small ξ. The negative sign ensures that ξ and ρ' have the same sign, even though density $\bar{\rho}$ decreases with height. The last expression was obtained using the assumed approximative profile of $\bar{\rho}$.

The application of relation between the density perturbation and the displacement (2.90) in the potential energy formula (2.89), using the equality $N_0^2 = g/H$, finally leads to the potential energy formula

$$E_p = \frac{1}{2}\rho_0 \frac{g^2}{N_0^2}\left(\frac{\rho'}{\rho_0}\right)^2. \tag{2.91}$$

The potential energy definition (2.91) (related to unit mass) was used for example in the study [42] of GWs observed by lidar. However, a great portion of the remote measurement techniques such as the Doppler radars or GPS radio occultation sounding rely on the refractive properties of the emitted signal on the inhomogeneities in the temperature field [43]. For this reason, many studies apply definition (2.91) with the relative perturbations of temperature T'/T_0 instead of relative perturbations of density ρ'/ρ_0 [44],[45],

$$E_p = \frac{1}{2}\rho_0 \frac{g^2}{N_0^2}\left(\frac{T'}{T_0}\right)^2 \tag{2.92}$$

or they study the GW spectra by calculating the power spectrum density of the relative temperature perturbations only [46].

The justification for the use of temperature perturbation is based on the perturbation form of the state equation for ideal gas in the linear perturbation theory.

If we divide the pressure, temperature and density field to the basic state p_0, T_0 and ρ_0 and a perturbation p', T' and ρ', we can write the state equation for both the basic and perturbed flow:

$$p_0 = \rho_0 R T_0, \tag{2.93a}$$

$$p_0 + p' = (\rho_0 + \rho')\, R\, (T_0 + T') \tag{2.93b}$$

with R being the specific gas constant. When we subtract the first equation from the second, after a few algebraic manipulations, assuming that the product $\rho' T'$ can be neglected, we get the state equation

$$\frac{p'}{p_0} = \frac{T'}{T_0} + \frac{\rho'}{\rho_0}. \tag{2.94}$$

In view of the previous state equation, it is clear that the density perturbations in (2.91) can be replaced by the temperature perturbations in (2.92), if the pressure perturbations are much smaller than the density and temperature perturbations. This does not have to be true in general. Therefore, we rather consider the potential energy in formula (2.92) just as a new definition motivated by the derivation above.

The vertical spectrum of the GW fluctuations has been studied also theoretically. The studies use the saturated spectrum theory, which assumes that a monochromatic wave becomes unstable if it causes negative potential temperature [47]. The spectra were analysed for fluctuations of different quantities. For the perturbations of temperature, which are relevant for the studies of the potential energy (2.92), the theoretical power spectral density of temperature perturbations has approximately the form

$$E_T(m) = \frac{N_0^4}{10 g^2 m^3}, \tag{2.95}$$

where g is the acceleration of gravity, N_0 is a typical value of Brunt-Väisälä frequency and m is the vertical wavenumber [44]. Less specified part of this theoretical spectrum is the factor 1/10, which, as well as the Brunt-Väisälä frequency, may vary with the altitude [48].

As we use the dependence on the inverse vertical wavelength λ_z instead of the vertical wavenumber m in the thesis, we need to modify the previous formula to

$$E_T(1/\lambda_z) = \frac{1}{(2\pi)^2} \frac{N_0^4}{10 g^2 \left(1/\lambda_z\right)^3}, \tag{2.96}$$

The denominator contains the second power of 2π and not the third, as one might expect, since the spectral density scales also by 2π when changing from the wavenumber notation to the notation with $1/\lambda_z$.

The last formula (2.96) still describes the power spectral density of temperature perturbation. By comparison with (2.92), rescaled by the density, we finally obtain the theoretical potential energy spectrum density,

$$E_{T,p}(1/\lambda_z) = \frac{1}{(2\pi)^2} \frac{N_0^2}{20 \left(1/\lambda_z\right)^3}. \tag{2.97}$$

For the spectrum evaluation, we also apply the non-equispaced Fourier transform, which is a generalization of the Fourier transform aimed at transforming data on non-uniform grids. In analogy with (2.72), the transform of a sequence of values a_n for $n = 0, \ldots, M-1$ corresponding to the sequence of points x_n, $n = 0, \ldots, M-1$, is defined by

$$\hat{a}_k = \sum_{n=0}^{M-1} a_n \mathrm{e}^{-2\pi i k x_n} \tag{2.98}$$

for an arbitrary frequency k.

2.3.3 Periodization Methods

For the computation of energy spectrum, we used DFT. However, DFT assumes that the data are periodic, which is not true for a local domain. Removal of these aperiodicities is essential to get correct, undistorted spectrum [49].

There are different approaches to this problem. The method we implemented for the spectrum computation is a detrending method presented by Errico in [50]. It is based on subtracting linear trend from each row and column of the data, where the slope is computed using the boundary values only. If the data values are denoted by $a_{i,j}$, $i = 1, \ldots, N$, $j = 1, \ldots, M$, we can write the slope of a line connecting the first and the last element in j-th column as

$$s_j = \frac{a_{N,j} - a_{1,j}}{N-1} \tag{2.99}$$

The values along the line are then modified by a line with the slope s_j so that the resulting column is periodic,

$$a'_{i,j} = a_{i,j} - i s_j + \frac{1}{2}\left(a_{N,j} - a_{1,j}\right) \tag{2.100}$$

The same procedure is applied also on rows.

This method can be generalized to subtract not only a linear function but also quadratic functions [51]. Another approaches are based on extension of the domain and multiplication of the data with a smooth function with zero on the boundary or to use the discrete cosine transform instead of DFT [52]

2.3.4 Effective Resolution

Numerical models do not correctly simulate effects in the atmosphere with scales similar to the grid size. In particular, it is not possible to resolve wave motions with frequency higher than Nyquist frequency, which is equal to the half of the sampling frequency. Moreover, in accordance with the dispersion relation derived in the Section 1.2.2, the frequency and the horizontal and vertical wave characteristics are interconnected. The limit of horizontal wavelengths that can be simulated by the models therefore does not depend only on the horizontal grid resolution, but also on the vertical grid resolution and on the time step. Instead of resolution of the model given by the mesh size, it is therefore necessary to use a so-called effective resolution, which is a limit value such that the smaller scales are not simulated correctly.

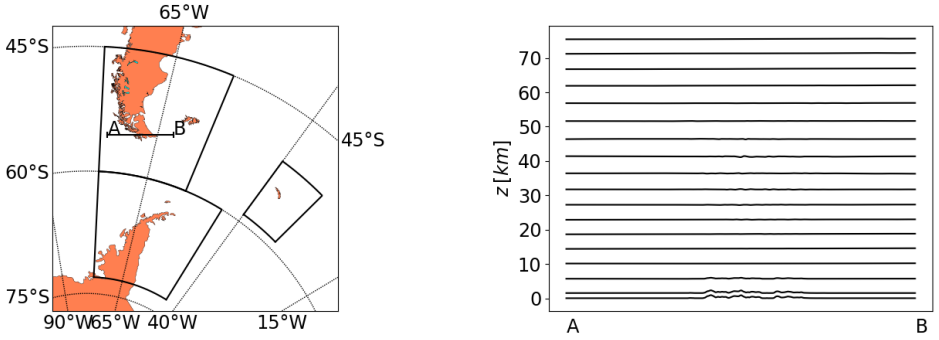

(a) Horizontal domain with marked subdomains. Line segment AB displays the cross-section depicted in Fig. 2.1(b).

(b) Vertical coordinates of the model data. The plot displays every tenth level.

Figure 2.1: Domain visualisation

Due to the numerical diffusion, error in interpolation and other numerical methods, kinetic energy at small scales is dissipated. As a result, the effective resolution can be recognized in the energy spectra as the scale where the spectrum starts to deviate steeply from the theoretical development [53].

2.4 Data

In the thesis, we test the methods on data from experimental simulations of Weather Research and Forecasting (WRF) Model, which solves fully compressible nonhydrostatic equations.

The data are given for a local domain covering parts of Southern America, Antarctica and the south-east of the Atlantic Ocean. For the majority of computations, we divide the domain into three GW hotspots, see Fig. 2.1(a). We will refer to the subdomains as Southern Andes, Antarctic Peninsula and South Georgia.

The used simulations, so far not published (a paper is in preparation [54]), have unusually high resolution. The horizontal resolution of the model is 3 km on the domain of about 3900 km in both horizontal directions. The simulation results are saved in simplified Lambert Conformal map projection on a sphere with radius 6370 km.

Vertical levels are defined using hybrid sigma-pressure vertical coordinate, which means that the levels follow the terrain at lower altitudes. At higher altitudes, the coordinate describes the pressure levels. The height of the simulated atmosphere is about 80 km and it is divided into 179 levels. The vertical coordinates are depicted in Fig. 2.1(b).

The data from simulation cover the period from 8$^{\text{th}}$ October to 19$^{\text{th}}$ October 2010 with the time step of 15 minutes.

2.5 Implementation

The scripts were implemented partly in Python and partly in NCAR Command Language (NCL). They were parallelized using the Python multiprocessing package and the program GNU parallel [55]. The scripts are enclosed with the thesis (see Attachment B for a brief description).

Because it is difficult to work with the non-equidistant vertical coordinate, for the majority of computations, the data are first interpolated on equidistant vertical levels with the distance 1 km. For this purpose, we use linear interpolation.

To be able to compute horizontal derivatives, in cases specified in the next subsections, we interpolate the data also horizontally to create a regular grid defined by values of latitude and longitude. This regridding is performed using the ESMF_regridding package in NCL in two steps. First, an interpolation matrix with weights that quantify impact of individual points in the source grid on the points in the destination grid is created. Because the horizontal grid does not vary in time, it suffices to apply this step for one time instant only. Second, the data are multiplied by the weight matrix to obtain the values on the destination grid. As the interpolation method, we use bilinear interpolation. Since the destination grid is defined by a maximal and minimal value of latitude and longitude, after the interpolation, we can work with a subdomain of the original domain only.

In several situations, we applied the two-dimensional Fourier transform even though the considered data are spherical and a more appropriate procedure would be to use the windowed spherical harmonics transform. The first reason is that in the atmospheric community, the usual approach is to use the Fourier transform for local domains [20], [56]. Since our aim is to compare our results with these studies, we do not change this methodology here. The second reason is that our aim is to study also the gravity waves with short wavelengths, for which we would need spherical harmonics with higher degree [57]. Using spherical harmonics, the problem would be therefore more computationally expensive. The transition to the spherical-harmonics approach will be subject of future studies.

2.5.1 High-pass Filter Method

The first method of the gravity wave separation we applied is the high-pass filter method described in Section 2.1.1.

The algorithm was implemented in both NCL and Python. It assumes that the data are vertically interpolated to the levels of constant altitudes. For each time step and for each vertical level, the following procedure is applied:

```
input: var, cutoff

var    = SubtractPlane(var)
coef   = Apply2DFFT(var)
coef   = MultiplyByResponseFunction(coef,cutoff)
smooth = ApplyInverse2DFFT(coef)
result = var - smooth
```

In the first step, a plane is fitted to the two-dimensional variable (`var`) and the fit is subtracted from the variable. The fitting uses the least squares method. In NCL, this is implemented by solving the system of normal equations, while

using every second point in both directions for the fitting only. The Python implementation uses the least-square solver in the package NumPy, which is based on the singular value decomposition.

The two-dimensional FFT in the second step and its inverse in the next-to-last step relies on build-in functions for real FFT in NCL or, in the Python script, on functions for real FFT in the package NumPy. We use real FFT, because the input data do not contain complex value and the real Fourier transform therefore provides the same information as the complete Fourier transform.

In the third step, the Fourier coefficients are multiplied by the response function defined by equation (2.1). Finally, we apply the inverse Fourier transform and subtract the smoothed data from the original data.

2.5.2 Active Wind Method

The algorithm for the method of active winds introduced in Section 2.1.2 was implemented in Python.

Just as in the high-pass filter method, the computation requires that the data are vertically interpolated on levels of a constant height. Additionally, an interpolation must be applied also in the horizontal directions, so that the rows and columns in the data represent the directions of constant latitudes and longitudes, as described above.

Using the vertically and horizontally interpolated data, the algorithm for computation of the active wind is a straight-forward evaluation of the right-hand side of equation (2.23). It can be written as follows:

```
input: p, theta, u, v, w, z, lat, lon

omega_a = AbsoluteVorticity(u,v,w,lat,lon)
T   = Temperature(p,theta)
rho = Density(p,T)
P   = ErtelsPotentialVorticity(rho,theta,omega_a,lat,lon)
phi = z*9.81
B   = BernoulliFunction(u,v,w,T,phi)
uia, via, wia = InactiveWind(rho,P,B,theta,lat,lon)
active  = [u-uia,v-via,w-wia]
```

The input of the algorithm is the pressure `p`, the potential temperature `theta`, velocity components `u`, `v` and `w`, the altitude `z`, the latitude `lat` and the longitude `lon`. It evaluates first the absolute vorticity using definition (2.11) and the formula for angular speed of Earth $\mathbf{\Omega} = (0, \Omega\cos\varphi, \Omega\sin\varphi)$. Then the temperature is evaluated using the combination of equations (2.7) and the relation (2.8). For the computation of density, we apply the ideal gas equation (2.6). The Ertel's potential vorticity is computed using its definition (2.18). Afterwards, we evaluate the geopotential and apply it to the computation of the Bernoulli function by the formula (2.10). Finally, the inactive wind component can be obtained using its definition (2.19), and the active part from (2.24).

The latitude and longitude values were used to evaluate the derivatives using formulas derived in the Attachment A. Further, we assumed that the altitude is much smaller than the radius of the Earth, so that we can approximate the radial coordinate in the derivatives by the radius of the Earth.

To avoid the problem with the change of the number of grid points in a direction after application of finite differences, we use central differences supplemented by the forward and backward differences at the edges.

Next, we describe how we compute forcing to the equations describing evolution of divergence and vorticity. Using the previous results and the same variable names, we can proceed by the following script.

```
input: active, theta, omega_a, lat, lon, z

wstar    = VelocityAlongIsentropes(active,theta,lat,lon,z)
zetastar = VorticityAlongIsentropes(omega_a,theta,lat,lon,z)
g1 = CalculateVectorG1(active,zetastar)
g2 = CalculateVectorG2(wstar,omega_a)
g  = g1 + g2
forcdiv  = Product([0,0,1],Curl(g,lat,lon))
forcvort = Div(g,lat,lon)
```

The first two quantities in the algorithm are computed using equations (2.32) and (2.33). For the computation of vectors $\mathbf{g}_1$ and $\mathbf{g}_2$, we use equations (2.35). Finally, the forcings are computed as the right-hand sides of (2.41).

2.5.3 Momentum Fluxes and Drag

The computation of the momentum fluxes and drag, implemented in NCL, also works with data for a subdomain defined by a range of latitudes and longitudes that are both vertically and horizontally interpolated.

The algorithm first evaluates the area of the subdomain using formula (2.61). For every altitude, the individual components are then computed using equations (2.60) and (2.62) – (2.66). The zonal drag can be then obtained as a sum of the components MWD_{xx}, MWD_{yx} and MWD_{zx}, the meridional drag is the sum of the components MWD_{xy}, MWD_{yy} and MWD_{zy}. Finally, the vertical flux of the zonal and meridional momentum is obtained using (2.67) and (2.68). The integration is performed as a sum of the values in respective horizontal direction(s) multiplied by the length of the step in latitudes or longitudes.

The algorithm therefore provides a value of the total drag and fluxes for the whole area of the domain at a given altitude and time instant.

2.5.4 Horizontal Energy Spectrum

Next, we describe our Python implementations of the computation of specific horizontal kinetic energy spectrum.

We start with data that are vertically interpolated to the levels of constant altitudes.

The first implementation is based on the Fourier transform of the velocity field. For simplicity, we assume to have two-dimensional fields of horizontal velocity components `u` and `v` with resolution `dx` at given altitude and time instant. The basic algorithm reads:

```
input: u, v, dx
```

```
Periodize(u,v)
ut,vt = Apply2DFFT(u,v)
deltat,zetat = ExpressFFTOfDivergenceAndVorticity(ut,vt)
K = WaveNumberSize(dx,u.dimension[0])
Eklz = EnergyFor2dWavenumbers(zetat,deltat,K)
EKz  = SumEnergyForWavenumbers(Eklz,K)
```

First, it computes the Fourier transform of periodized velocity components, proceeds using equations (2.78) and (2.79) to get the DFT of vorticity and divergence and prepares the two-dimensional array of the horizontal wave-number size using (2.82). Then it computes $E^z_{k,l}$ using equation (2.81) and finally sums it up employing equation (2.85).

The periodization technique applied on the velocity components in the first step is described in Section 2.3.3. For a two-dimensional variable, the structure of the procedure is

```
input: var

for c in columns(var):
   s=CalculateSlope(c)
   SubtractSlope(c,s)
for r in rows(var):
   s=CalculateSlope(r)
   SubtractSlope(r,s)
```

The slope is obtained from formula (2.99) and the subtraction is described by equation (2.100).

The second algorithm for the spectrum computation is a slight modification of the previous one:

```
input: u, v, dx

delta,zeta   = DivergenceAndVorticity(u,v)
deltat,zetat = Apply2DFFT(delta,zeta)
K = WaveNumberSize(dx,u.dimension[0])
Eklz = EnergyFor2dWavenumbers(zetat,deltat,K)
EKz  = SumEnergyForWavenumbers(Eklz,K)
```

Instead of starting by the Fourier transform of velocity components, it evaluates the divergence (2.77) and vorticity (2.76) using a finite difference scheme.

As for the finite differences in the first step of the algorithm, we compare three different schemes, the forward differences, the central differences and the five-point difference scheme. For a sequence $\{f_k\}$, these difference schemes can be defined as

$$\Delta f_k = f_{k+1} - f_k, \tag{2.101a}$$

$$\Delta_c f_k = \frac{1}{2}\left(f_{k+1} - f_{k-1}\right), \tag{2.101b}$$

$$\Delta_f f_k = \frac{1}{12}\left(-f_{k+2} + 8f_{k+1} - 8f_{k-1} + f_{k-2}\right). \tag{2.101c}$$

To be able to compare the different methods even though the differences are not defined for a few rows and columns near the boundary, we evaluate all the spectra for the common inner part only.

2.5.5 Vertical Energy Spectrum

The evaluation of the vertical spectrum of the specific potential energy was also performed in Python.

We first compute the temperature from the definition of potential temperature (for instance combination of equations (2.7) and (2.8)), express the Brunt-Väisälä frequency from equation (1.6) and evaluate the specific potential energy using the definition (2.92) divided by ρ_0, so as to be able to compare our results with other studies.

The filtration of the temperature field to the basic state and perturbation, which is needed for the formula evaluation, is done by fitting polynomials to the subsets of data obtained from individual air columns. The same filtering is performed also on the potential temperature needed for the computation of Brunt-Väisälä frequency, as, because of the absence of hydrostasy assumption, it cannot be obtained from the background field of temperature.

After the potential temperature is evaluated in every point, we apply the one-dimensional FFT to the square root of the potential energy values in individual air columns. The vertical spectrum is then obtained by multiplication of the Fourier transform result with its complex conjugate. In the last step, the result is multiplied by the considered altitude range and divided by the square of the number of points within the range, so that it does not depend on these variables.

This procedure can be written in a simplified way, starting with the potential temperature `theta`, the pressure `p` and the altitude `z`, as follows:

```
input: theta, p, z

T=Temperature(theta,p)
T_b=FitPolynomial(T)
theta_b=FitPolynomial(theta)
T_p=T-T_b
N2=BruntVaisalaSquared(theta_b,z)
Ep=SpecificPotentialEnergy(N2,T_p,T_b)
Epst=Apply1DFFT(sqrt(Ep))
Ept=Epst*conjugate(Epst)
Ept_dens=PSD(Ept)
```

The previous procedure with the Fourier transform can be applied only if the data are equidistant in the vertical direction. This property can be reached by linear interpolation of the non-equidistant data to a regular grid. However, such procedure might modify the spectrum by smoothing the perturbations. For this reason, we also test the previous algorithm with application of the non-equispaced Fourier transform instead of the Fourier transform.

As for the implementation of the Fourier transform generalization, we use the Non-equispaced fast Fourier transform (NFFT) algorithm described as Algorithm 3 in article [58]. It is based on the FFT and on approximations based on a window function. We used its implementation in the Python package nfft [59].

2.5.6 Effective Resolution and GW Range

The scripts searching for the effective resolution and the range of the GW wavelengths were both implemented in Python.

As their input, we use the horizontal kinetic energy spectra `EkzAll` found by the first algorithm in Section 2.5.4, the vector of horizontal wavenumbers `k` and the time in which we evaluate the effective resolution or the GW range.

The effective resolution of the data in a given time step at a studied altitude is found by the following simple algorithm described in detail below:

```
input: EkzAll, k, time

EksAll= SmoothenOverTime(EkzAll)
Eks   = log(EksAll[time])
ks    = log(k)
line  = FitLineToSpectrum(Eks,ks,(30,80))
sigma = StandardDeviation(line,Eks,ks,(30,80))
j     = IndexOf(k,30)+1
while (abs(line.evaluate(ks[j]) - Eks[j])<4*sigma):
   j=j+1
effk  = k[j-1]
```

In the first step, the specific horizontal horizontal kinetic energy spectra at a given altitude are smoothed over the time interval of 15 hours using the moving mean. This interval length corresponds to the lower bound on gravity wave frequency, as derived in Section 1.2.2 and removes a part of the oscillations from the spectra. These averages are characterized by the time specification in the middle of the interval.

Next, we take the smoothed spectrum at a given time and we fit a line to the part of the spectrum in the log-log plot corresponding to the wavelength range 30 – 80 km. We further evaluate the standard deviation of the interpolated line from the original spectrum, which we then use as a threshold to determine the point in which the fitted line starts to depart from the spectrum values. We assume that this point is the sought effective resolution.

In the remainder of the chapter, we deal with the algorithm for the specification of the upper bound for wavelengths at which are GW dominant, written as a pseudocode at the end of the chapter. It can be divided into two parts.

In the first part, we preprocess the energy spectra to obtain uniform sampling. The energy spectra are again smoothed over time. To simplify the explanation, we then take just one of these spectra. Because the upper bound on the GW wavelengths cannot be smaller than the effective resolution, only the part of the spectra with wavelengths above the effective resolution is considered. Within the preparatory work, we further evaluate the logarithm of wave-numbers and the energy spectrum to represent the values in the log-log plot. This, however, changes the distribution of the values of the wave-numbers to non-uniform. We therefore apply linear interpolation to the logarithmic values. Finally, we resample the values uniformly by linear interpolation.

The second part contains the main loop of the algorithm. It divides the sampled points into two sequences of consecutive points, each starting at one end of the array containing the interpolated wavenumbers. The algorithm initializes the left sequence with the leftmost array point, the right sequence with the rightmost array and iteratively adds points to one of the sequences until all points belong to one of the sequences. At each step, it is necessary to choose, whether we add a point to the left sequence or to the right one. To this end, we try to add a

neighbouring point to both sequences and using the new sequences, we fit two lines to the energy values. For the right sequence, we fix the slope of the fitted line to $-5/3$, a constant introduced in Section 2.3.1, to ensure the right part is dominated by GWs. We evaluate the distance of the lines from the energy values at the added points. We compare this error for the right and the left sequence, and we decide to add a point to the sequence for which the error is smaller. When there are no points left, the position between the sequences is considered to be the upper bound of GWs.

The main structure of the algorithm is written compactly below. Apart from the horizontal specific kinetic energy spectra at all times `EkzAll`, vector of wavenumers `k` and a selected time `time` as in the previous algorithm, the input of the algorithm is also the effective resolution `effk`.

```
input: EkzAll, k, time, effk

EksAll= SmoothenOverTime(EkzAll)
Eks   = EksAll[time][0:Index(effk)]
ks    = k[0:Index(effk)]
Ek_un,k_un = InterpolateToUniform(log(Eks),log(ks))

l_edge = 1
r_edge = (length(ks)-1)-1
slope  = -5/3
while (l_edge<r_edge):
  l_line =Interpolate(Ek_un[0:l_edge+1],k_un[0:l_edge+1])
  r_line =Interpolate(Ek_un[r_edge-1:end],k_un[r_edge-1:end],slope)
  l_error=ErrorAtNewPoint(l_line,Ek_un,k_un,l_edge+1)
  r_error=ErrorAtNewPoint(r_line,Ek_un,k_un,r_edge-1)
  if (l_error<r_error):
     l_edge = l_edge+1
  else:
     r_edge = r_edge-1

kmin = l_edge
```

3. Results

In this chapter, we begin by presenting the properties of the data – the horizontal and vertical energy spectra, derive effective resolution of the model and the upper range of the GW wavelengths (i.e. the longest GW wavelenghts) that are present in the data. Then we focus on the high-pass filter method, its dependence on the cutoff length and we present an improved method that uses the GW range based on the results of our analysis. Finally, we show all the results for two specific time instants, including the results from the active wind method.

3.1 Effective Resolution and GW spectra

3.1.1 Horizontal Energy Spectrum

We calculated the spectra by four methods – a method using the Fourier transform of the velocity components and, to be able to verify the results, three methods based on Fourier transforms of divergence and vorticity calculated by finite difference schemes: forward differences, central differences and five-point differences. The resulting spectra of the methods differ slightly for short and long wavelengths, see Fig. 3.1(a).

For smaller wavenumbers, all the spectra calculated by finite differences coincide and their energy are slightly higher than by the method without finite differences. A similar result was presented in article [36], Figure 3, where, contrary to our results, the method without finite differences has higher energy. The difference between the methods decreases with decreasing wavelength.

We assume that the differences at high wavenumbers are caused by two effects.

The first one is the effect of the boundary. In the processed WRF simulation, boundary conditions cause abrupt changes of gradient of velocity field at the boundary. This makes it less reasonable to use the detrending method described in Section 2.3.3 and, using the method that calculates FFT of velocity components, it leads to oscillations in spectrum for the short wavelengths (Fig. 3.12(a)). The other methods are not so affected by this phenomenon as the vorticity and divergence that are transformed to the Fourier space are near zero both in wave-less parts of the domain and near the boundaries, and no detrending is being applied. The oscillations vanish if we consider only a subdomain inside the original domain.

The second effect explains the differing results of finite differences for shorter wavelengths. It is grounded in the smoothing properties of certain finite-difference schemes. Specifically, the central differences can be computed as arithmetic mean of two subsequent values of forward differences. The five-point method cannot be expressed as a mean of forward differences so easily, but as it considers more points for computations, it also causes some smoothing. The central-difference scheme and the five-point scheme thus smooth out small-scale patterns that are contained in the results of the forward differences and consequently, the methods show lower energy at shorter horizontal wavelengths.

Further, we dealt with the decomposition of the horizontal kinetic energy into the divergent and rotational component. An example of the decomposition for

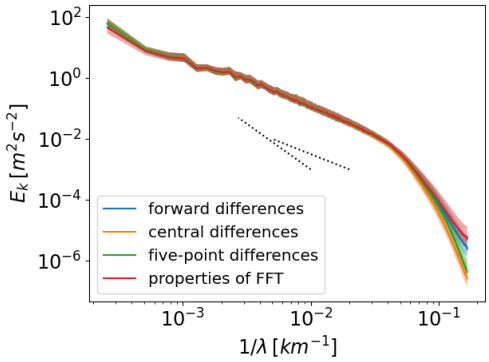

(a) Comparison of different methods of horizontal spectra computation. The dotted lines display the theoretical slopes -3 and -5/3.

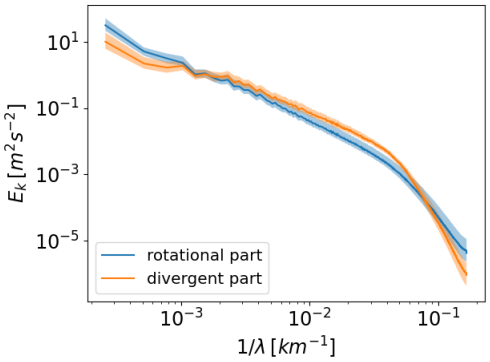

(b) Decomposition of the spectrum into the divergent and vortical part. The spectrum was evaluated by the method that uses properties of FFT (red line in Fig. 3.1(a)).

Figure 3.1: Horizontal spectrum at the altitude 40 km. Solid line denotes the median value over the time period, filled regions denote the regions between the lower and upper quartile.

the altitude of 40 km can be shown in Fig. 3.1(b) evaluated again using the entire domain. As expected, the dominant component of energy in the studied range of wavelengths is the divergent one connected with the presence of GWs. However, the rotational component of energy connected probably mainly with geostrophic modes [5] is present in the full range of wavelenghts and, as expected, it dominates the spectrum for wavelenghts longer than about 1000 km. It also dominates the spectrum at shortest wavelenghts, which may be connected with the fact that the ability of the model to resolve those modes does not depend critically on the vertical resolution of the model.

Apart from evaluating the spectra for the whole domain, we also visualized it for the subregions around the Southern Andes, South Georgia and Antarctic Peninsula (figure not shown). Even though, for example, the region of South Georgia is relatively small, the resulting spectra are similar to the spectra for the whole domain.

3.1.2 Vertical Energy Spectrum

Before presenting the results regarding the vertical specific potential energy spectrum observed in the data, we start by studying the theoretical relation (2.97).

As already mentioned, the major problem with the relation (2.97) is the dependence of the Brunt-Väisälä frequency N_0 on the altitude. In other studies dealing with the spectrum computation, the spectra are usually computed using data from smaller altitude range due to the availability of such data and the Brunt-Väisälä frequency is considered to be constant at this range (e.g. [44], [60]).

However, in our data, N_0 changes significantly (Fig. 3.2(a)). It first increases from values around zero in the lower levels to the maximal value, approximately 0.025 s^{-1} in the middle stratosphere. From this level, it decreases back to values around 0.015 s^{-1} in the middle mesosphere. Above, it is approximately constant.

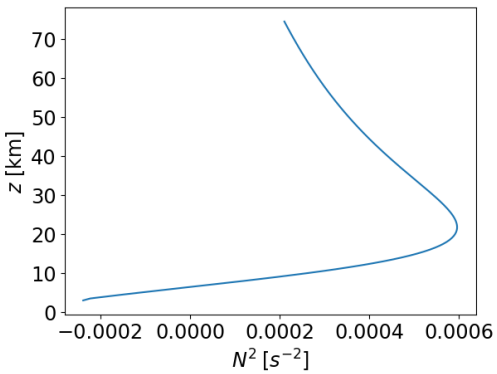

(a) Vertical profile of the squared Brunt-Väisälä frequency.

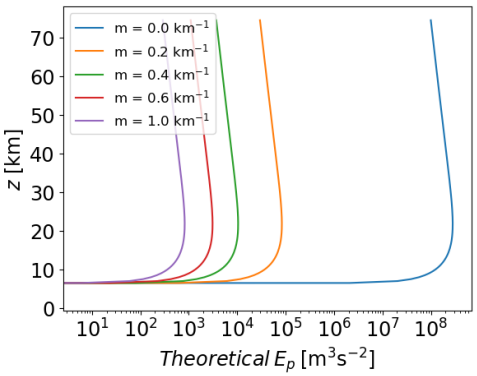

(b) Dependence of the theoretical potential energy spectral density (2.97) on the altitude via the vertical profile of Brunt-Väisala frequency for different reciprocal vertical wavelengths.

Figure 3.2: Dependence of theoretical potential energy of the basic flow on altitude at a time step, averaged over the Antarctic Peninsula subdomain. Perturbations were separated from the profile by fitting polynomials to the potential temperature.

To understand the effect of the variability of N_0, we studied the dependence of the theoretical energy given by (2.97) on the altitude, using the vertical profile of the Brunt-Väisälä frequency observed in the data (Fig. 3.2(b)). For a constant vertical wavenumber, the theoretical potential energy changes rapidly near the levels of zero N_0. These very steep changes stop about the level of approximately 10 km. In the higher altitudes, the theoretical energy first increases with altitude up to the maximal value at approximately 20 km, after which it decreases. Even though the magnitude of the changes is much smaller for the logarithm of the energy in the altitudes above 10 km, the value of the energy can still change by a half of order of magnitude. For the power spectrum of temperature fluctuation, the dependence of the theoretical spectral density (2.96) on the altitude is even more significant due to the presence of fourth power of the Brunt-Väisälä frequency.

The motivation of the potential energy definition (2.92) similarly assumes nearly constant Brunt-Väisälä frequency. Therefore, we cannot evaluate the vertical spectra using all model levels at once, although the model data contain information about seventy-kilometre altitude range. Instead, we divide the levels into three altitude ranges, 10 – 25 km, 25 – 50 km and 50 – 73 km. The restriction of the lower level to 10 km is necessary due to the quick increase of N_0 below this level.

Within these ranges, the Brunt-Väisälä frequency still cannot be considered constant. However, because the vertical resolution of the model is about 400 m, we cannot use much shorter ranges in order to have enough values at each range.

The scaling used for computation of the spectrum density from the square of the Fourier transform of the square root of potential energy is for the implementation that uses NFFT instead of FFT not entirely correct, since the levels are not equidistant. On the other hand, if we consider only a range of the levels,

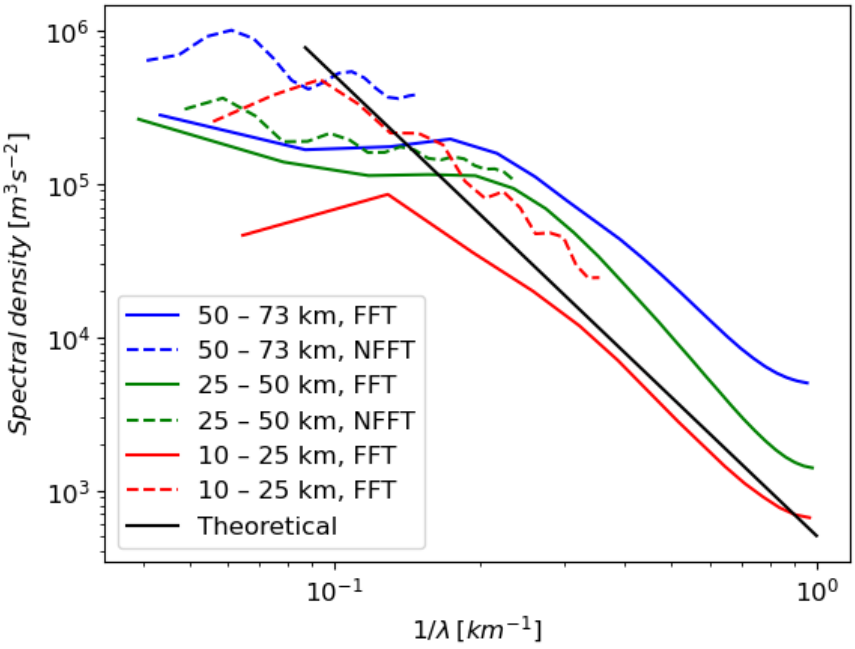

Figure 3.3: Vertical spectrum averaged over the Antarctic Peninsula subdomain.

their distances do not vary significantly (see Fig. 2.1), and an approximation by the mean distance seems reasonable. Even though this approximation reduces the benefit of using NFFT over the linear interpolation, the method based on the linear approximation might cause larger errors by interpolating levels that are far away from the model levels. A better method for the estimation of the spectral density without similar assumptions is to use a periodogram method [61], which we plan to use in future research.

Vertical specific potential energy spectrum averaged over time and over the subdomain Antarctic Peninsula is depicted in Fig. 3.3. The plot contains the spectra computed from three different altitude ranges, using the non-equidistant data with the NFFT method and the linearly interpolated data with the FFT. We visualised also the theoretical slope (2.97) for $N_0 = 0.02\ s^{-1}$. However, as discussed above, the slope contains a significant uncertainty connected with the dependence of the Brunt-Väisälä frequency on the altitude. Therefore, we cannot rely on the correctness of this line.

For the shortest vertical wavenumbers, the spectral density of potential energy increases with the wavelengths. The slope in this part of the spectra approximately corresponds to the slope of the theoretical dependence for GWs. The increase is interrupted by the drop of the potential energy for motions with vertical wavelengths of about 5 km.

Further, note the change of the vertical potential energy spectra shape for the longest wavenumbers. Similarly to the concept of effective resolution introduced for the horizontal spectra, this deviation from the theoretical slope could be related with the model to simulate waves with short vertical wavelengths. For Antarctic Peninsula subdomain, in Fig. 3.3, this vertical effective resolution can be determined as approximately 1.2 km for all the altitude ranges.

The next observation that can be done in Fig. 3.3 is that the energy evaluated from the non-equidistant data is higher than the energy evaluated after the linear

interpolation. This is consistent with the assumption that the linear interpolation causes apparent decrease of the wave activity. On the other hand, we consider the wavy shape of the spectra computed by the NFFT method to be rather an artefact of the method, as the structure does not change much in time. The NFFT method evaluated the spectra also for smaller wavenumbers. Nevertheless, as we are not interested in the contributions to the potential energy by effects with approximately zero frequency, we do not plot this part of the spectra.

The difference between the spectra computed using FFT and NFFT can also be partially explained as a consequence of polynomial fitting, which is necessary for division of the temperature and the potential temperature into the mean values and perturbation field. For the NFFT method using the non-equidistant data, we always used all the levels of the model for the fitting. For the method with FFT, we interpolated the levels at the range $6 - 73$ km and the polynomial fitting was therefore applied on this range only. The method working with non-equidistant data might therefore specify the perturbation field at the edges of the intervals more correctly due to the access to the information from outside the intervals. This could explain the fact that in Fig. 3.3, the two method are close to each other in the middle altitude range, whereas they differ significantly for the bottom and top altitude ranges.

Finally, the figure indicates the dependence of the energy on the altitude range. Apart from the NFFT computation in the lowest range, the spectra evaluated at higher altitudes have generally higher energy than the spectra evaluated at lower altitudes. This could be caused either by the increase of wave amplitudes due to the decrease of density with altitude, or it can be an effect of the vertical profile of the Brunt-Väisälä frequency.

Spectra averaged over other subdomains (Fig. 3.4) look very similar to spectra in Fig. 3.3. Again, the energy computed by the FFT method is in the part of the spectra that corresponds to GWs lower in lower altitudes. The difference between the FFT and NFFT method is also qualitatively the same as for the Antarctic Peninsula subdomain.

On the other hand, one can observe a difference between the subdomains in the spectrum for the lowest altitude range. Either the vertical effective resolution corresponds to a much longer wavelength (around 2 km), or the resolution is the same, but the GW spectrum is not saturated for wavelengths approximately between 1 and 2 km.

3.1.3 Effective Resolution and GW Range

Next, we study the time evolution of the effective resolution and the upper bound of the saturated part of the GW spectrum in the heights of 5 km, 20 km and 40 km.

As for the effective resolution, determining it was generally simple, as the expected decrease of the horizontal kinetic energy for small scales was generally well distinguishable. This is the reason why we did not apply a more involved algorithm for the recognition of the value. On the other hand, in some cases the change of the spectrum is more gradual (e.g. bottom middle plot in Fig. 3.5) and the specification therefore contains some uncertainty.

Even though the effective resolution should theoretically be constant for the

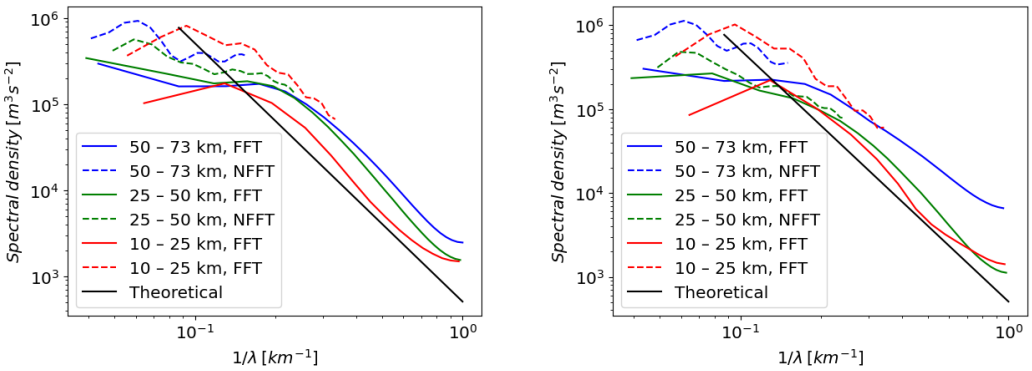

(a) Southern Andes subdomain.

(b) South Georgia subdomain.

Figure 3.4: Vertical energy spectra averaged over other subdomains.

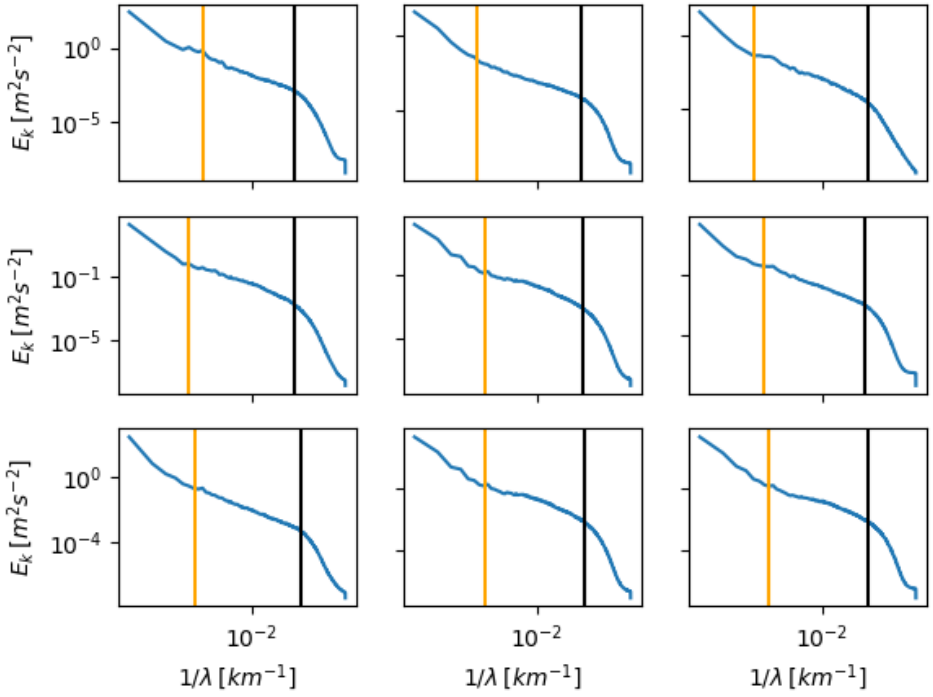

Figure 3.5: GW range and effective resolution at 20 km. Example of spectra from nine randomly chosen time instants. The black vertical line denotes the effective resolution, the orange vertical line denotes the upper bound of the horizontal wavelengths with dominant GW.

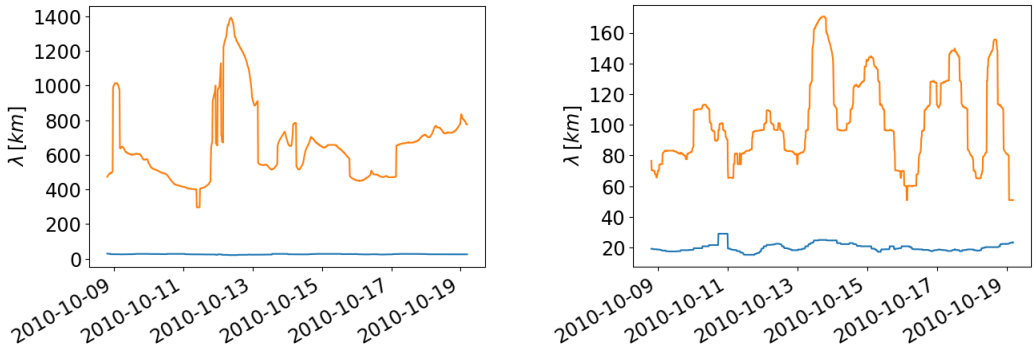

(a) Altitude 20 km.

(b) Altitude 5 km.

Figure 3.6: Time evolution of the GW range. The orange line is the upper bound of the horizontal wavelengths with dominant GW, the blue line represents the time evolution of the effective resolution.

simulation settings, the determined value can vary in time not only due to the imprecise algorithm, but also due to the absence of small-scale waves in the given time step or conversely, due to the presence of unusually large portion of small-scale waves that compensate for the decrease of energy. The time evolution of the effective resolution is plotted in Fig. 3.6. For the altitude of 5 km, the variations of the effective resolution are nicely visible. The flat maximum in the plot is caused by the fact that the algorithm seeking the effective resolution assumes that GW with wavelengths 30 – 80 km are always present, which is not satisfied in these time instants and it therefore fits a line to a spectrum with a different slope.

The time mean of the effective resolution further depends on the height. For the altitude of 5 km, the effective resolution was determined as (20 ± 3) km, whereas the effective resolution at 20 km and 40 km are (26 ± 2) km and (25 ± 1) km, respectively. A possible reason might be that the model has a better vertical resolution in the lower levels than in the upper ones (Fig. 2.1), which can cause that more waves are resolved in the bottom levels.

The effective resolution of the WRF model was estimated, for example, in article [39] to approximately seven times the horizontal grid resolution. More recently, it was studied in article [62]. The authors determined that the effective resolution for a simulation with the horizontal grid resolution 3600 m is approximately 30 km. Both these results are consistent with our results.

The reason why determining of the upper bound on the GW part of the spectrum is more complicated can be seen in Fig. 3.5. The problem is that the horizontal kinetic energy spectra are not smooth in the wavelengths for which the bound is sought. Therefore, if we applied a similar algorithm as for the determining of the effective resolution, based on fitting a line to a part of the spectrum with GWs, the found wavelength would be much smaller than the correct wavelength, as the algorithm would terminate on the first random departure. These bumps in the spectra can be caused partly by the insufficient number of points for longer wavelengths due to the logarithmic scale. On the other hand, they could also indicate the presence of GWs with a dominant wavelengths and they should, in such a case, be included in the part of the spectra with GWs.

The results regarding the decomposition of energy into the divergent and rotational part in Section 3.1.1 suggest an alternative method of the upper bound specification that would look for an intersection of the two parts of the energy spectrum. The intersections seems to correspond well to the wavelengths found by our algorithm. However, due to the problematic determination of the intersection of the rough parts of the spectra, this method would face the same difficulties as the method we applied.

Apart from the effective resolution, Fig. 3.6 also visualizes the time evolution of the upper bound at the altitudes of 5 km and 20 km. Clearly, at the altitude of 5 km, the wavelengths at which GWs lose their dominance are much shorter than at the altitude of 20 km. This is a consequence of the fact that at 5 km, the atmosphere is generally not stable, which is a necessary condition for the preservation of an initial vertical perturbation and subsequently for the creation of GWs.

3.2 High-pass Filter Method

In this section, we demonstrate the high-pass filter method, its properties and we propose a new, improved, method.

The procedure of the high-pass filter method is illustrated in Fig. 3.7. The part 3.7(b) was obtained from 3.7(a) by subtracting a fitted plane. Subsequent filtering in the Fourier space leads to the part 3.7(c).

At first sight, the method successfully reveals a wave-structure in the middle of the domain. As we consider the data in the computation as a flat square domain, not respecting its spherical character, and we do not apply any periodization technique, the method creates incorrect values of the perturbation field near boundaries. However, this is not a problem for our computations since we subsequently study only the values from the subdomains marked in Fig. 2.1, which do not contain the incorrect boundary parts of the domain.

3.2.1 Sensitivity to Cutoff

To verify the reliability of the high-pass filter method, we study its dependence on the cutoff length.

To this end, the high-pass filter method was applied to the data at the altitudes 5 km, 20 km and 40 km for cutoff lengths between 250 km and 1550 km with the step of 50 km. The resulting fields were used to evaluate the momentum fluxes and mountain wave drags, as described in Section 2.5.3, for the three subdomains.

The high-pass filter method is a suitable method, if the values of the MWDs and MFs do not depend on the cutoff length, i.e. if their derivatives with respect to the cutoff length equal zero. We thus computed the derivative of the quantities with respect to the cutoff length using finite differences. Finally, these derivatives were rescaled by the median of the quantities over the time and cutoff length, so that the significant dependence on the cutoff length is easily recognizable from the values.

In Figure 3.8, we show the time evolution of the dependence of the zonal and meridional component of the MWD on the cutoff length at the altitude of 20 km for the three subdomains. In the plots, we would like to see a band of white color

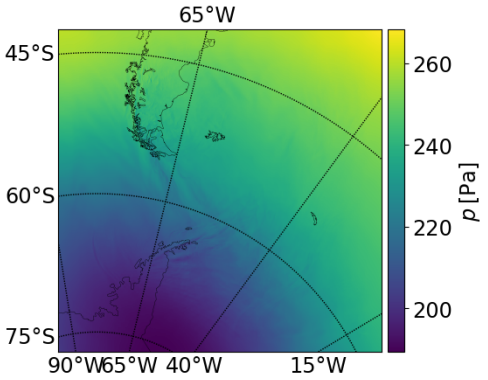

(a) Pressure field at the altitude of 40 km.

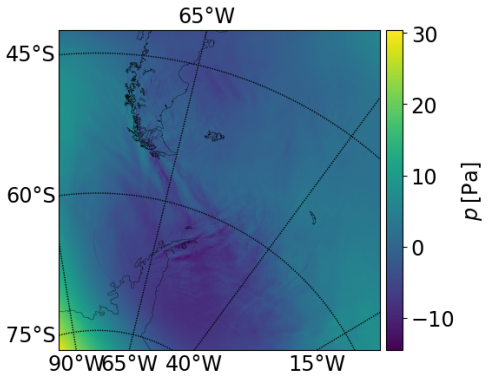

(b) Pressure field from Fig. 3.7(a) after subtraction of a fitted plane.

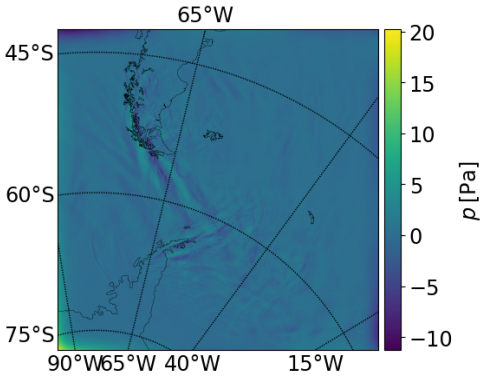

(c) Perturbation of the pressure obtained by the high-pass filter method with cutoff length 500 km.

Figure 3.7: Illustration of the high-pass filter method on the pressure field at the altitude of 40 km.

indicating that it is possible to determine a range of cutoff lengths, such that the method does not depend on the parameter at any time instant.

For the Southern Andes subdomain, the method indeed seems to be independent on the cutoff for some intermediate values of the cutoff range in the period between 14^{th} and 17^{th} October. Nevertheless, it does depend on the cutoff length significantly for other days and all cutoff lengths.

As for the subdomain of South Georgia, the dependence is similar to the dependence at Southern Andes. Between approximately 15^{th} and 17^{th} October, the method does not depend on the cutoff length so substantially for a range of smaller cutoff lengths. Outside this range and for other days, the sensitivity is, however, much higher than in the case of Southern Andes.

The last pair of plots in Fig. 3.8 for the Antarctic Peninsula subdomain looks differently. In this case, the sensitivity is rather lower for smaller wavelengths up to 15^{th} October, after which there is no cutoff range that could be considered to be the correct one. Nevertheless, the values differ less than for the previous subdomains.

Considering other altitudes, the results can be summarized as follows.

For most subdomains and altitudes, both the zonal and meridional MFs appear to be dependent on the cutoff length for smaller cutoff values only (up to 600 km). Strong dependence on the cutoff even for higher cutoff values can be observed in all cases at the altitude of 5 km and for the zonal component, and also for some subdomains at the altitude of 20 km.

The dependence of the MWD components on the cutoff length vary also with the altitude. Just as for the MFs, the dependence is generally more significant at lower altitudes. Again, at the altitude of 40 km, it is reasonable not to use cutoff lengths up to 600 km, due to higher dependence on the cutoff length. Unlike the MFs, for certain time instants, the MWD is slightly dependent on the cutoff length also for higher cutoff lengths. For the altitudes 5 km and 20 km, the MWD components exhibit dependence on the cutoff length for the whole considered range of the cutoff lengths for all considered subdomains.

Assuming that the behaviour of the high-pass filter method depends on the wavelength of the waves present in the subdomain, the very slight similarity between the plots for Southern Andes and South Georgia in Fig. 3.8, shifted in time, might be related to the observation that the longest waves from the Southern Andes subdomain propagate into the subdomain of South Georgia. In contrast, the subdomain of Antarctic Peninsula stays interconnected to the other subdomains by shorter waves.

A more detailed examination of the situations with high and low sensitivity to the cutoff length for the Southern Andes subdomain at the altitude 20 km will be presented in Section 3.4.

3.2.2 Improved Method

To overcome the problem of the discovered dependence of the high-pass filter method, we propose an improved version of the method. The idea is to use the information obtained from the horizontal kinetic energy spectra to specify a correct value of the cutoff length at each time step.

The first option for the improved algorithm is to use the upper bound of the

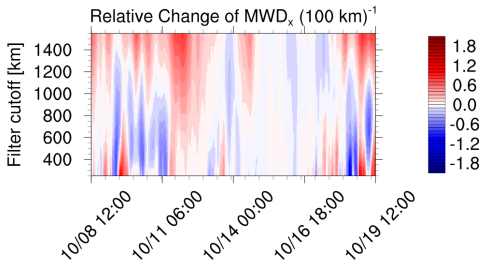

(a) Derivative of MWD_x with respect to the cutoff, rescaled by the median. Evaluated for the Southern Andes subdomain.

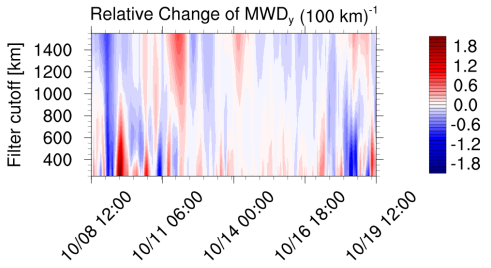

(b) Derivative of MWD_y with respect to the cutoff, rescaled by the median. Evaluated for the Southern Andes subdomain.

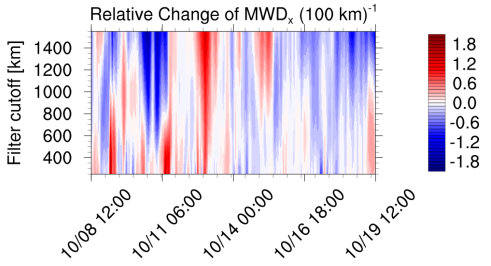

(c) Derivative of MWD_x with respect to the cutoff, rescaled by the median. Evaluated for the South Georgia subdomain.

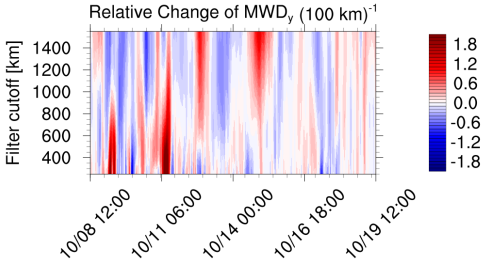

(d) Derivative of MWD_y with respect to the cutoff, rescaled by the median. Evaluated for the South Georgia subdomain.

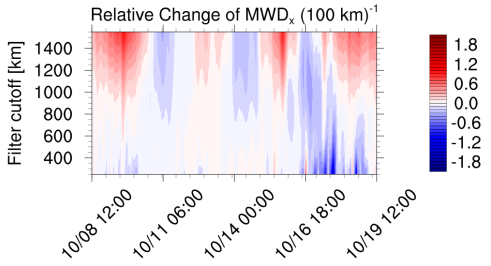

(e) Derivative of MWD_x with respect to the cutoff, rescaled by the median. Evaluated for the Antarctic Peninsula subdomain.

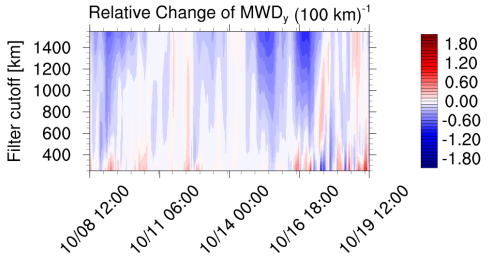

(f) Derivative of MWD_y with respect to the cutoff, rescaled by the median. Evaluated for the Antarctic Peninsula subdomain.

Figure 3.8: Dependence of MWD at the altitude of 20 km on the cutoff length. The colours code the relative MWD change with respect to the median of the absolute value of MWD computed over time and cutoff length. The two colours close to white represent the change of the MWD component smaller than 10 % of the median if the cutoff length is increased by 100 km.

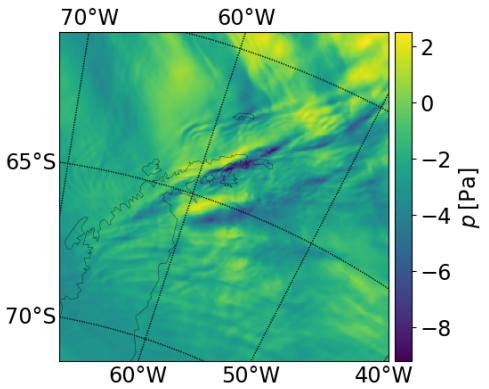

(a) Perturbation field of the pressure obtained by high-pass filter method with the cutoff length computed from the horizontal kinetic energy spectrum.

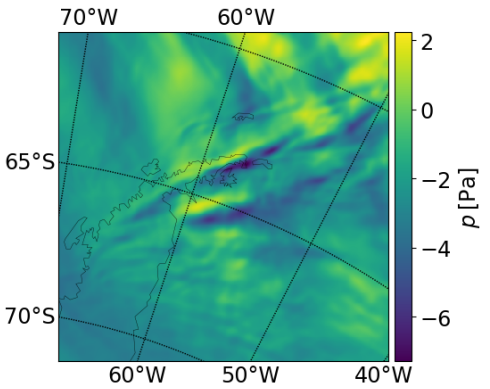

(b) Perturbation field of the pressure obtained by combination of high-pass filter and low-pass filter with the same cutoff length for high-pass filter as in Fig. 3.9(a) and the cutoff length for the low-passed filter set on the basis of the effective resolution.

Figure 3.9: Comparison of high-pass filter and a combination of high-pass and low pass filter, displayed on a detail of the pressure field from Fig. 3.7(a).

GW wavelength and the effective resolution of the model obtained in Section 3.1.3 to specify the cutoff lengths to the high-pass filter and to a low-pass filter. The definition of the low pass filter is completely analogous to the definition of the high-pass filter, using the response function (2.1).

However, we argue that the removal of the wavelengths shorter than the effective resolution is not appropriate. Although the effective resolution means that the waves with wavelengths shorter than this threshold are not correctly resolved by the model, it does not necessarily mean that there are no such waves. The effective resolution is evaluated from the data from the entire domain. Locally, there might be present waves with horizontal wavelength smaller than the determined effective resolution that are resolved by the model due to the sufficiently long vertical wavelength. By application of the low-pass filter, we would lose the information from these waves.

This is illustrated in Fig. 3.9 by comparing a detail from the pressure field from Fig. 3.7(a). In Fig. 3.9(a), only the high-pass filter with the cutoff found on the basis of the horizontal kinetic energy spectrum is applied. Fig. 3.9(b) uses both the high-pass filter and the low-pass filter. The images show that the pressure field after applying only the high-pass filter method contains some wave-like structures that are undesirably removed by the low-pass filter.

For this reason, the only modification of the original high-pass filter method is that we set the cutoff value dynamically, using the wavelength at which GWs lose their dominance.

To avoid confusion, recall that we do not use the term cutoff length exactly for the shortest wavelength that is removed from the data in the high-pass filter method. Instead, these two values must be in our notation converted from one to another in view of formula (2.3).

The improved method is compared with the original high-pass filter method

for a constant value of the cutoff length 500 km. This value of the constant is chosen so that it lies in the range of the cutoff lengths that is assumed to be applicable in the study [20], similar to the constant cutoff values repeatedly used in literature [63], [64], [65].

These two methods, evaluated again using MFs and MWDs on the subdomains at different altitudes, in the majority of situations coincide or the time evolutions of the studied quantities are at least similar.

For the altitude 5 km, the quantities computed by the improved method are generally closer to zero, as the method takes into account the fact that GWs are dominant for much shorter wavelengths only. For the altitudes 20 km and 40 km, the values are rather further from zero, which can be explained by the same reasoning. However, due to the stronger variations of the GW range in time, this effect is not so pronounced.

In Fig. 3.10, these two methods are compared using the values of the zonal and meridional component of MWD in the altitude 20 km on different subdomains. These plots are consistent with Fig. 3.8 and the range of GW wavelengths at the altitude 20 km in Fig. 3.6(a).

One of the most noticable differences between the methods can be seen on 12^{th} October for the zonal MWD component in Southern Andes (Fig. 3.10(a)). The high-pass filter method in this case computed values of the drag slightly below zero, whereas the improved method found values up to 2 m $\text{s}^{-1}\text{day}^{-1}$, which is the largest value of the zonal component of MWD in the subdomain. Regarding the meridional MWD in Southern Andes (Fig. 3.10(b)), one of the more visible differences between the methods is also for this day, even though the difference is not so significant as for the zonal component.

For the subdomain of South Georgia (Figs. 3.10(c) and 3.10(d)), a similar, significant discrepancy between the methods can be identified for a latter period, rather on 12^{th} October in the evening. As already mentioned in the previous section, this time shift could correspond to the time necessary for the wave propagation between the subdomains.

The magnitude of the difference around 12^{th} October can be so large due to the long horizontal wavelengths considered to belong to GWs (Fig. 3.6(a)), as the methods then use completely different cutoff values. However, for the Antarctic Peninsula subdomain, the cutoff difference for computation of the meridional component of MWD (Fig. 3.10(f)) on this day does not have an impact on the results of the methods. The results of the methods for zonal component of MWD for Antarctic Peninsula (Fig. 3.10(e)) are not the same, it is nevertheless smaller than for the other subdomains.

For other days, the cutoff length derived from the wavelength is for nearly all the time steps also larger than the constant cutoff 500 km. Nonetheless, the difference between the methods is generally not so large. We mention for example the time period between 15^{th} and 17^{th} October, when the methods produce the same results for nearly all cases in Fig. 3.10. This is consistent with the time period of weaker sensitivity identified in Fig. 3.8.

In the previously mentioned time period of less pronounced sensitivity, the magnitudes of MWD were relatively small. This is, however, not a necessary condition for the methods to produce similar results. A counterexample is for example the end of the simulation, at which both the methods consistently end

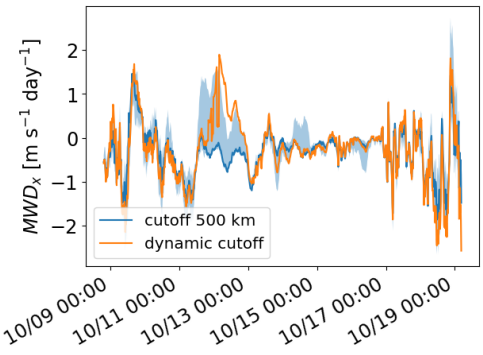

(a) Zonal drag component, Southern Andes.

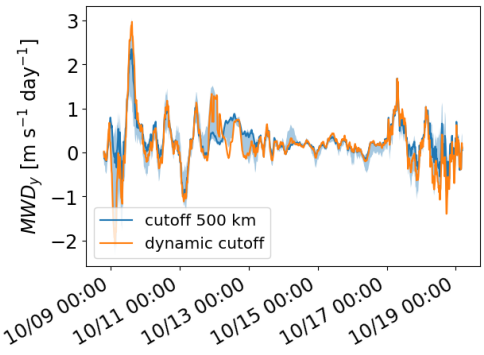

(b) Meridional drag component, Southern Andes.

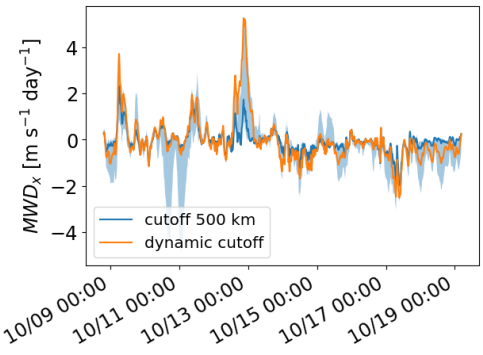

(c) Zonal drag component, South Georgia.

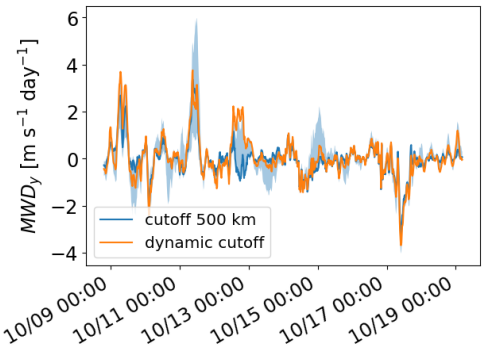

(d) Meridional drag component, South Georgia.

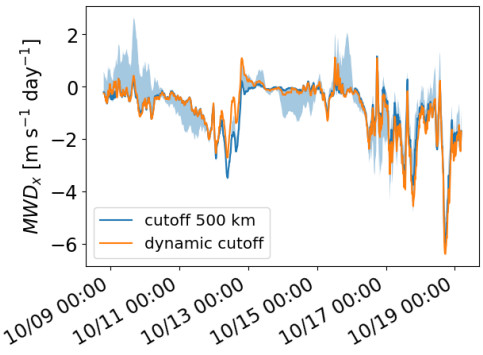

(e) Zonal drag component, Antarctic Peninsula.

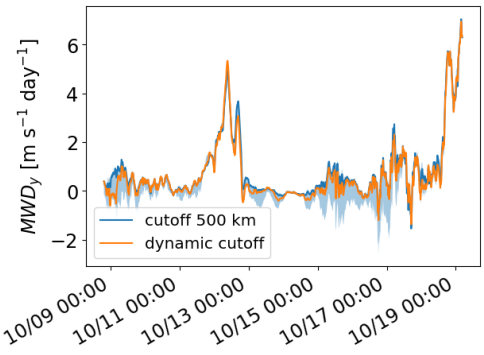

(f) Meridional drag component, Antarctic Peninsula.

Figure 3.10: Comparison of the improved method and high-pass filter method with constant cutoff. The orange lines visualize the time evolution of MWD computed using the wave perturbation from the improved method. The blue lines describe the evolution of MWD using the high-pass filter method with constant cutoff length 500 km. The filled blue regions represent the possible values of MWD in individual times for the cutoff range 250 – 1550 km.

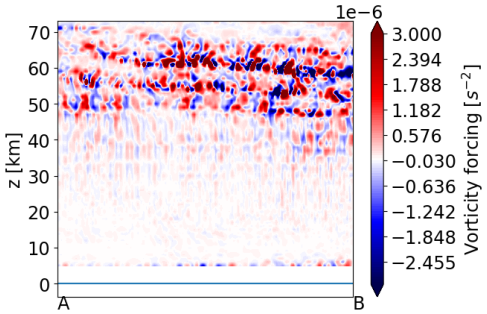

(a) Vorticity forcing computed by the active wind method.

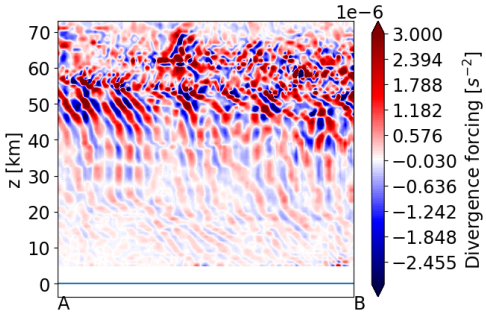

(b) Divergence forcing computed by the active wind method.

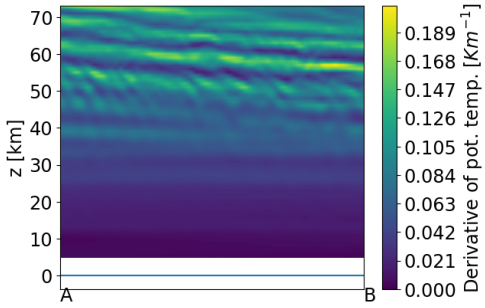

(c) Vertical derivative of the potential temperature.

Figure 3.11: Illustration of the active wind method – vertical cross-section along a segment of 58$^{\text{th}}$ parallel south, above the Drake Passage.

with relatively large values of MWD.

Altogether, in the comparison of the methods, there are time intervals, at which the values are approximately the same, and time intervals, at which they differ completely. These cases will be studied in Section 3.4 in more detail.

3.3 Active Wind Method

In this section, we will show some properties of the active wind method.

Since we were not able to separate the velocity perturbations corresponding to GWs from the perturbation fields, we cannot compare the MF and MWD resulting from the active wind method with the high-pass filter methods. Instead, we use the active wind method to help explaining the difference between the original high-pass filter method and its improved version in Section 3.4.

Examples of vertical cross-sections of the divergence and vorticity forcing are depicted in Fig. 3.11. Up to the altitude of about 45 km, the vorticity forcing exhibit a weak small-scale structure. In the divergence forcing, sections with positive and negative values form backward slanted stripes that are supposed to be related to GWs. The size of the forcing generally grows with the altitude.

Cross-sections from different regions of the domain look very similarly. The largest difference is that the vertical section in Fig. 3.11 is above the sea surface only. Therefore, we cannot see any GWs generated over orography, as for example in Fig. 3.13(b), but only their horizontal propagation. The second difference is

in the altitude of the level at which the structure of the results notably changes.

To explain the behaviour of the method in the upper atmosphere, vertical profile of the vertical derivative of potential temperature for the same cross-section as the divergence and vorticity forcing is shown in Fig. 3.11(c). We can see that the quantity significantly changes with the altitude in the upper levels and its value is often very close to zero. The layers with zero potential temperature gradient can be a sign of evolving vertical overturning turbulence due to the GW dissipation. However, in the derivation of the forcing terms, we assumed it is non-zero (see definitions (2.32) and (2.33)).

In the lower atmosphere, the values of the vertical derivative of the potential temperature are also very small. Nevertheless, this does not cause problems since their gradient is much smaller.

Comparison of the derivative of potential temperature with the vorticity forcing in Fig. 3.11(a) reveals that the nearly horizontal bands of the vorticity forcing with greater magnitude indeed correspond to the bands of very small vertical derivative of the potential temperature. A similar structure is visible also in Fig. 3.11(b), where the similarity with the plot of vertical derivative of the potential temperature is, however, not so apparent due to the generally larger values of the divergence forcing in the upper levels.

We therefore consider the different behaviour of the method at higher altitudes to be an error due to the unsatisfied assumption. The performance of the method, in the regions with near zero potential temperature gradients has to be tested in the future work and it is of particular interest due to the link to GW dissipation. In the next section, we plot only the lower altitudes.

3.4 Case Study

In this section, we study in detail two time instants of the simulation, using the previous results. The first represents the situation when the high-pass filter method with constant cutoff length 500 km and the improved method give very similar results, and the high-pass filter method does not depend on the cutoff length. The second example is chosen such that the methods differ significantly.

For the choice of these time instants, we utilized the results depicted in Figs. 3.10(a), 3.10(b), 3.8(a) and 3.8(b). We therefore focus on the situation in the subdomain of Southern Andes for the MWD. To avoid the trivial case, in which the improved method uses the same cutoff length as the original one, we do not choose the days with the lowest upper bound of the GW wavelength in Fig. 3.6(a).

To understand the differences between these situations, we study the horizontal and vertical spectra and the results obtained from the active wind method.

Even though we focus on a subdomain only, the horizontal kinetic energy spectrum is always evaluated for the whole domain, as the subdomain is too small and the spectrum computed purely from the data on the subdomain would not represent the longest GW wavelengths correctly. This is not a problem, because for the chosen cases, the agreement or disagreement of the methods on a subdomain approximately corresponds to the agreement or disagreement in other subdomains. Also, the studied Southern Andes locality represents one of the

larger hotspots in the domain, so the spectrum for the entire domain reflects the wave activity on this subdomain.

In the next subsections, we are refering to a single time step with better correspondence of the high-pass filter methods and a single time step with worse correspondence. Nevertheless, we observed the general properties of the spectra described in the next subsections also in other time instances with similar differences between the high-pass filter methods.

3.4.1 Example 1

The first selected time instant is from 15$^{\text{th}}$ October 2010, 00:00. In this case, the results of the high-pass filter methods are very similar. The plots characterizing this situation are depicted in Fig. 3.12.

First, we focus on the horizontal specific kinetic energy spectrum in 3.12(a). The shape of the spectrum is quite similar to the average spectrum at the altitude 20 km. Note the fast transition between the part of the spectra with dominant rotational energy and the part with dominant divergent energy. This enables relatively good specification of the wavelength bound that is used for the improved high-pass filter method. The found wavelength is approximately 650 km, which corresponds to the cutoff length slightly smaller than 920 km. Fig. 3.12(a) suggests that the utilization of the cutoff length 500 km, denoted by solid grey vertical line in the plot, instead of the found cutoff length, denoted by black line, leads to the inclusion of smaller portion of the spectrum, in which GWs dominate. However, this difference does not seem to have a significant impact on the hight-pass method results. The majority of MF is probably carried by the part of the spectrum at shorter wavelengths.

In the vertical specific potential energy spectrum density in Fig. 3.12(b), we do not see a straight part corresponding to the saturated part of the GW spectrum. In comparison with the average vertical spectrum 3.3, its changes with the wavenumber are gradual. The theoretical spectrum does not fit onto the computed spectrum quantitatively, either. This could, however, be caused by the incorrect specification of the multiplicative parameters in the formula for the theoretical spectrum. Considering only the slope of the theoretical spectrum, it seems that GWs with shorter wavelengths (smaller than 2 km) are rather missing. The maximal wavelength that might be attributed to GWs is about 5 km. Together with the hypothesis from above that the MFs are dominated by waves with shorter horizontal wavelengths this is suggesting that the waves will have rather vertical phase line orientation, an expectable result for mountain waves over a steep terrain. Nevertheless, these numeric wavelength specifications are not very clear due to the discrepancy with the theoretical spectrum.

The vertical structure of the waves can be also viewed in the vertical cross-section of the divergence forcing field, evaluated using the active wind method (Fig. 3.12(d)). Above mountains, slightly slanted columns of positive and negative values of the divergence forcing are generated. Even though one vertical cross-section cannot represent the whole domain, the near vertical alignment of the phase lines supports the above made hypothesis about the shorter horizontal wavelengths. In the altitude about 10 km, the forcing is attenuated, suggesting dissipation of the primer GWs. Higher up the forcing is pronounced again with

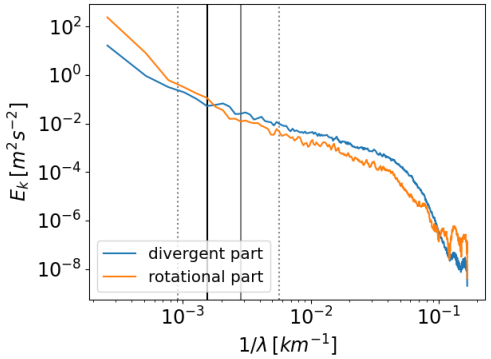

(a) Horizontal spectrum of kinetic energy at the whole domain at the altitude of 20 km. Grey line denotes the wavelength corresponding to the cutoff 500 km, black line corresponds to the cutoff of the improved method. The region between the dotted lines is the range of wavelengths at which we tested the dependence on the cutoff.

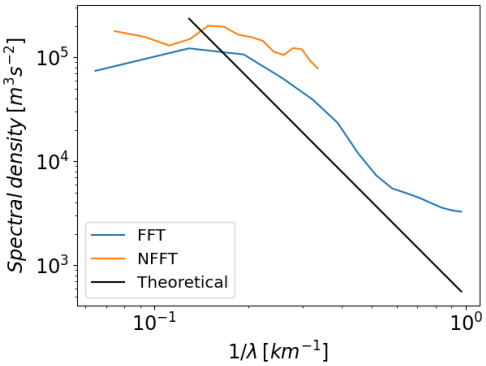

(b) Vertical spectrum of potential energy evaluated at the altitude range 10 – 25 km , averaged over the subdomain of Southern Andes. Theoretical line corresponds to the Brunt-Väisälä frequency 0.02 s^{-1}.

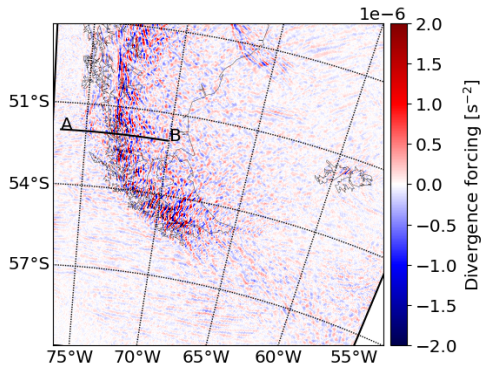

(c) Horizontal intersection of the forcing to the divergence equation, evaluated by the active wind method at the altitude of 20 km.

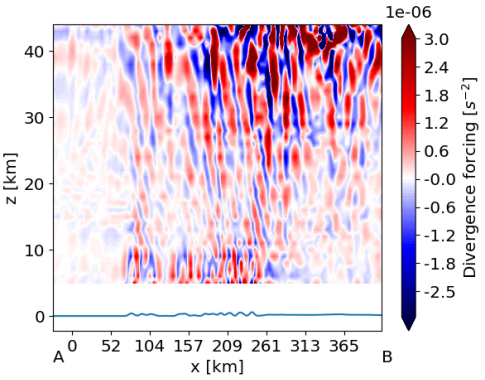

(d) Vertical cross-section of the forcing to the divergence equation, evaluated by the active-wind method at the cross-section denoted in Fig. 3.12(c). Blue line at the bottom represents the topography.

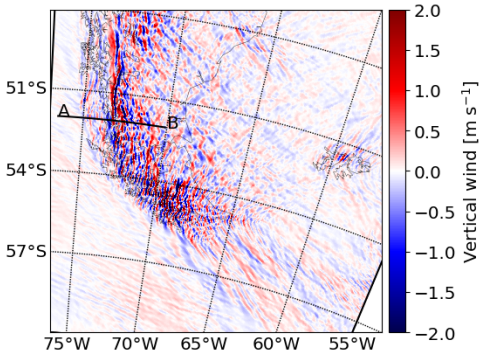

(e) Vertical velocity at the altitude of 20 km.

Figure 3.12: Situation on 15th October 2010, 00:00, at the subdomain of Southern Andes. The length of the line segment AB in Figs. 3.12(c) and 3.12(e) is approximately 440 km.

possible contribution of secondary generated GWs.

The attenuation of GWs' structure in the altitude range 10 – 25 km can explain the specific shape of the vertical spectrum, since the spectrum is computed using exactly this altitude range. Moreover, from Fig. 3.12(d), the vertical wavelength of the wave motion can be estimated to be 5 km, which is in accordance with the information obtained from spectral analysis.

In the horizontal cross-section of the divergence forcing (Fig. 3.12(c)), evaluated by active wind method, a small-scale structure apparent particularly above the mountain ranges is visible. On the other hand, the method does not provide us any waves with longer horizontal wavelengths. Such waves are, however, confirmed to be present in the data by the horizontal kinetic energy spectrum. This so far unpublished fact that the short waves dominate the forcing has a logical reasoning. Namely, it can be anticipated that the time derivative of the divergence at a point is higher if the divergence changes faster for shorter waves with shorter frequencies.

To obtain waves with longer wavelengths from the forcing terms, a spatial or temporal averaging would be necessary. This property might nevertheless become very useful for future research, as exactly the shortest waves are the waves that must be parametrised in weather prediction models. Using the forcing to the divergence equation, it seems to be possible to study their propagation and distribution in the domain in detail.

In our case, using a detail of Fig. 3.12(c), the forcing to the divergence equation can be used to confirm the effective resolution of the model around 25 km.

To visualize also waves with longer wavelengths, the horizontal cross-section of the vertical velocity is shown in Fig. 3.12(e). Apart from the small-scale structure above the mountains similar to the structure obtained by the active wind method, the vertical velocity plots makes visible also waves with horizontal wavelengths roughly estimated 100 km to 300 km, situated at the south of the subdomain. However, as these wavelengths correspond to the cutoff length smaller than the considered value 500 km, they will be treated by the two high-pass filter methods similarly and they are not expected to cause any difference between the results.

3.4.2 Example 2

The second time instant that we study, in which the high-pass filter methods provide different results, is 12^{th} October 2010 at 00:00. For the study of this situation, we use plots in Fig. 3.13.

Again, we start by the horizontal specific kinetic energy spectrum, visualized in Fig. 3.13(a). In contrast to the previous case (Fig. 3.12(a)), there is a range of wavelengths at which the divergent and rotational part have similar energy. This might cause problems, since we either do not include a significant part of the divergent spectrum, assumed to belong to GWs, or we work with the rotational part of the spectrum.

On the other hand, the effect of the rotational part of the spectrum on the MFs and MWDs is not so clear. It is natural to assume that the vortical modes produce smaller vertical velocity perturbations than GWs. From this, one could deduce that, for example for the zonal drag component in view of equations (2.57), the

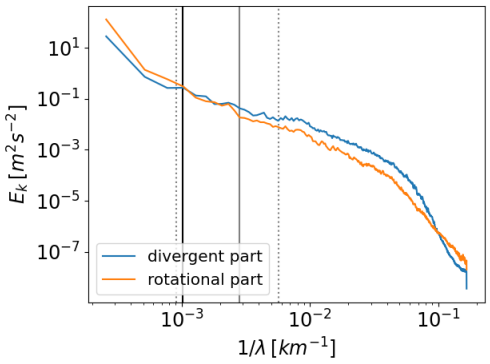

(a) Horizontal spectrum of kinetic energy at the whole domain at the altitude of 20 km. Vertical lines have the same meaning as in Fig. 3.12(a).

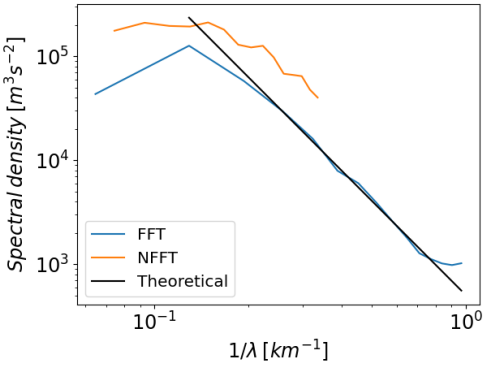

(b) Vertical spectrum of potential energy evaluated at the altitude range 10 – 25 km, averaged over the subdomain of Southern Andes. Theoretical line corresponds to the Brunt-Väisälä frequency 0.02 s^{-1}

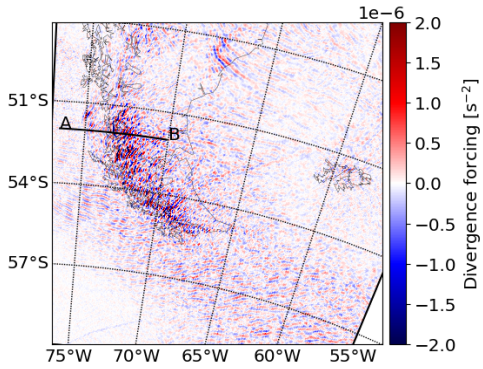

(c) Horizontal intersection of the forcing to the divergence equation, evaluated by the active wind method at the altitude of 20 km.

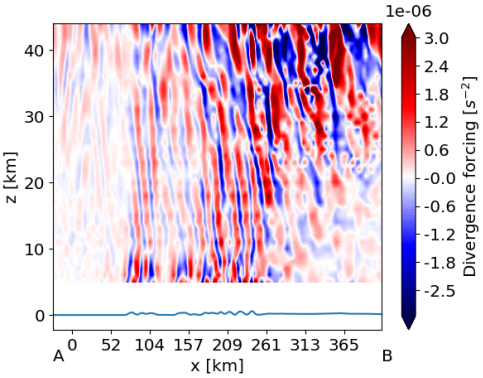

(d) Vertical cross-section of the forcing to the divergence equation, evaluated by the active-wind method at the cross-section denoted in Fig. 3.13(c). Blue line at the bottom represents the topography.

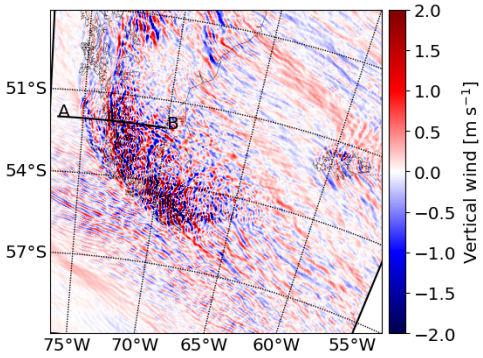

(e) Vertical velocity at the altitude of 20 km.

Figure 3.13: Situation on 12$^{\text{th}}$ October 2010, 00:00, at the subdomain of Southern Andes. The length of the line segment AB in Figs. 3.13(c) and 3.13(e) is approximately 440 km.

dominant MWD_x components for these modes are the components MWD_{xx} and MWD_{yx}. In the observed MWD_x, the component MWD_{zx} has, however, larger magnitude than the other two. Admitting also that GWs can contribute to some extent to all three parts, this consideration suggests that the effect of vortical modes on MWD components could be relatively small. A further research in this direction is needed.

Returning to the studied situation in Fig. 3.13, the horizontal wavelength specified by our algorithm as the upper bound of the spectrum part with dominant GWs is 980 km, which corresponds to the the cutoff length approximately 1390 km. The difference in the cutoff lengths is therefore relatively big. Nevertheless, as can be deduced from Fig. 3.8, this cannot be the only reason for which the improved method provides different results than the original high-pass filter method in this time instant and not so different results in the time instant in the previous section.

One of the most notable differences between the plots in Fig. 3.12 and Fig. 3.13 is in the vertical potential energy spectral densities, because the vertical spectrum in Fig. 3.13(b) indeed follows the line for the theoretical spectrum.

Therefore, we can specify the maximal vertical wavelength to be between 5 km and 7 km. A more exact specification of the maximal vertical wavelength is not possible due to the sparsity of points in this part of the spectrum; this could be improved by taking larger altitude range for the spectrum computation.

The minimal vertical wavelength that can be associated with GWs that are correctly simulated by the model is in this case slightly above 1 km, which is smaller than this wavelength in the previous case.

The different form of the vertical spectra in Fig. 3.12 and Fig. 3.13 can be also anticipated from the vertical cross-section of the divergence forcing (Fig. 3.13(d)). The backward slanted stripes of positive and negative divergence forcing are in this case above the mountains more pronounced and there is no attenuation in the lower stratosphere.

The broader parts of the vertical cross-section of the divergence forcing might indicate that only the waves with longer wavelengths are present in this part of the domain. This hypothesis is consistent with Fig. 3.13(e), where the wave motion changes from the small-scale waves to waves with slightly larger scales around the point B. In the horizontal cross-section of the divergence forcing, this transfer is expressed as a decrease of the magnitude of the forcing.

As for the horizontal cross-section of the divergence forcing in general, the two time instants also differ. In particular, in Fig. 3.13(c), there is more divergence forcing also near the mountain ranges, not only above them. That is, the second chosen time instant contains more wave activity with horizontal propagation of short waves. Similarly to the previous time instant, this plot further confirms the previously determined effective resolution.

In this case, the plot of vertical velocity (Fig. 3.13(e)) is very interesting. First, as in the divergence forcing, we can see a variety of waves with smaller scales in the south part of the domain, even with slightly modified direction compared to Fig. 3.13(e). This is attributed to the generally chaotic situation with high wave activity and mixing of the wavelengths in the vertical velocity plot.

The most interesting part are, however, the waves in the east, which are well

pronounced and have relatively long wavelengths that could be approximated up to 500 km. With such a wavelength, the wave would be considered to belong to gravity waves by the improved high-pass filter method, but by the original method with cutoff length 500 km, the wave would be added to the mean flow. Assuming a significant part of the MF is carried by this wave, it could cause the discrepancy between the high-pass filter methods.

Conclusion

Internal gravity waves (GWs) are wave-like motions within a stably stratified fluid. Impacting the middle atmosphere by interactions with other motions and by the energy and momentum transport and deposition, they constitute an important component of the atmospheric dynamics.

As GWs act even on very small scales, considerable part of their spectrum is not resolved by the global circulation models. Hence, their effects must be supplied to the models by parametrizations, for which it is necessary to estimate the contribution of GWs to the momentum and energy budget.

This could be achieved by thorough observations of GWs in the atmosphere. However, observations of GWs in the atmosphere also face several difficulties. In addition, to calculate the quantities for the parametrizations, the GWs' perturbations to all the velocity components must be specified. Specifically, we cannot settle for a perturbation field of temperature or vertical velocity, which would be sufficient for visualization of GWs.

The objective of the thesis was to study the GW diagnostic methods in data obtained from high-resolution simulations, as high-resolution models resolve larger portion of the GW spectrum and so they can be used to estimate the quantities for the parametrizations.

In the theoretical introduction, we first introduced GWs and their properties, the dispersion relation and an example of a polarization relation. Subsequently, we re-derived the methods applied in the thesis in detail. A special care was dedicated to the derivation of the active wind with the identification of the forcing terms in the equation of divergence and vorticity and to the derivation of the formulas for momentum flux and mountain wave drag computation in spherical coordinates.

In the practical part of the thesis, we worked with a large dataset from an experimental simulation of the WRF model with the horizontal resolution of 3 km.

First, we studied the properties of the data. To specify, which GWs are present in the simulation, we studied the horizontal and the vertical spectra. In the horizontal spectra, we identified the effective resolution and the maximum horizontal wavelength, at which GWs dominate. The determined effective resolution of the model lies approximately between 20 and 25 km, depending mostly on the altitude. In the altitude of 5 km, GWs dominate up to horizontal wavelengths only about 100 km. In higher altitudes, the maximum dominant horizontal wavelength ranges between 400 and 1300 km. The vertical spectra revealed that the data contain GWs with vertical wavelengths in average up to 5 km.

Next, we dealt with the high-pass filter method. By evaluation of the momentum flux and mountain wave drag for GWs filtered from the data using different values of the cutoff length, we determined the sensitivity of the method to the parameter. The results showed that in most situations, the results change significantly with the cutoff length, proving that the constant cutoff adds considerable uncertainty to the momentum flux and mountain wave drag estimates. The sensitivity is less pronounced for higher altitudes.

Based on the results of the cutoff sensitivity, we implemented a new, improved version of the high-pass filter method. It uses the maximum wavelength with

dominant GWs, obtained from the horizontal spectra.

Further, we applied a method for visualisation of GWs, the active wind method. The output of the method, up to the altitude about 40 – 60 km, seems to describe the wave structure of GWs realistically at small scales by showing their non-dissipative contribution to the forcing of the divergence of the flow. The performance of this method in the range of GW dissipation is left for future research.

In the final part of the thesis, all the previous approaches were utilized to study two selected time instants. The situations, in which the original high-pass filter method with constant cutoff length and the improved version give similar and different results, were compared. We observed the differences mainly in the different shape of the vertical spectrum and the size of the maximal horizontal wavelength, for which GWs dominate. Consequently, it seems that the original high-pass filter method is consistent with the improved method for time instants with lower wave activity with lower contributions from horizontally propagating GWs into the domain only.

The possible further research in this area includes studying other methods for local domain and the GW diagnostic methods suitable for the global data. The ability to correctly distinguish GWs from the background further enables us to study the physical mechanisms of the internal gravity waves, their interaction with background or with other wave-type motion.

Bibliography

[1] František Pechala. *Příručka dynamické meteorologie*. Academia, Praha, 1991.

[2] James Holton. *An introduction to dynamic meteorology*. Elsevier Academic Press, Burlington, MA, 2004.

[3] David C. Fritts and M. Joan Alexander. Gravity wave dynamics and effects in the middle atmosphere. *Reviews of geophysics*, 41(1), 2003.

[4] David G. Andrews, James R. Holton, and Conway B. Leovy. *Middle atmosphere dynamics*. Academic Press, 1987.

[5] Ulrich Achatz, Bruno Ribstein, Fabian Senf, and Rupert Klein. The interaction between synoptic-scale balanced flow and a finite-amplitude mesoscale wave field throughout all atmospheric layers: weak and moderately strong stratification. *Quarterly Journal of the Royal Meteorological Society*, 143(702):342–361, 2017.

[6] Bruce R. Sutherland. *Internal gravity waves*. Cambridge University Press, Cambridge New York, 2010.

[7] Annelize Van Niekerk, Irina Sandu, and Simon B. Vosper. The circulation response to resolved versus parametrized orographic drag over complex mountain terrains. *Journal of Advances in Modeling Earth Systems*, 10(10):2527–2547, 2018.

[8] Riwal Plougonven, Alvaro de la Cámara, Albert Hertzog, and François Lott. How does knowledge of atmospheric gravity waves guide their parameterizations? *Quarterly Journal of the Royal Meteorological Society*, 146(728):1529–1543, 2020.

[9] Marvin A. Geller, M. Joan Alexander, Peter T. Love, Julio Bacmeister, Manfred Ern, Albert Hertzog, Elisa Manzini, Peter Preusse, Kaoru Sato, Adam A. Scaife, et al. A comparison between gravity wave momentum fluxes in observations and climate models. *Journal of Climate*, 26(17):6383–6405, 2013.

[10] Adam A. Scaife, Neal Butchart, Christopher D. Warner, David Stainforth, Warwick Norton, and John Austin. Realistic quasi-biennial oscillations in a simulation of the global climate. *Geophysical Research Letters*, 27(21):3481–3484, 2000.

[11] Jadwiga H. Richter, Fabrizio Sassi, and Rolando R. Garcia. Toward a physically based gravity wave source parameterization in a general circulation model. *Journal of the Atmospheric Sciences*, 67(1):136–156, 2010.

[12] M. Joan Alexander, Marvin Geller, Charles McLandress, Saroja Polavarapu, Peter Preusse, Fabrizio Sassi, Kaoru Sato, Stephen D. Eckermann, Manfred Ern, Albert Hertzog, et al. Recent developments in gravity-wave effects in

climate models and the global distribution of gravity-wave momentum flux from observations and models. *Quarterly Journal of the Royal Meteorological Society*, 136(650):1103–1124, 2010.

[13] M. Joan Alexander. Gravity waves in the stratosphere. *The Stratosphere: Dynamics, Chemistry, and Transport*, 190:109–121, 2010.

[14] Robert A. Vincent and Albert Hertzog. The response of superpressure balloons to gravity wave motions. *Atmospheric Measurement Techniques*, 7(4):1043–1055, 2014.

[15] Guerman Poler, Raphaël F. Garcia, Daniel C. Bowman, and Léo Martire. Infrasound and gravity waves over the Andes observed by a pressure sensor on board a stratospheric balloon. *Journal of Geophysical Research: Atmospheres*, 125(6):e2019JD031565, 2020.

[16] Damian J. Murphy, Simon P. Alexander, Andrew R. Klekociuk, Peter T. Love, and Rhea A. Vincent. Radiosonde observations of gravity waves in the lower stratosphere over Davis, Antarctica. *Journal of Geophysical Research: Atmospheres*, 119(21):11–973, 2014.

[17] Benoit Cushman-Roisin and Jean-Marie Beckers. *Introduction to geophysical fluid dynamics: physical and numerical aspects*. Academic press, 2011.

[18] Ulrike Lohmann, Lüönd Felix, and Fabian Mahrt. *An introduction to clouds: from the microscale to climate*. Cambridge University Press, 2016.

[19] Robert A. Vincent and M. Joan Alexander. Gravity waves in the tropical lower stratosphere: An observational study of seasonal and interannual variability. *Journal of Geophysical Research: Atmospheres*, 105(D14):17971–17982, 2000.

[20] Christopher G. Kruse and Ronald B. Smith. Gravity wave diagnostics and characteristics in mesoscale fields. *Journal of the Atmospheric Sciences*, 72(11):4372–4392, 2015.

[21] Lena Schoon and Christoph Zülicke. A novel method for the extraction of local gravity wave parameters from gridded three-dimensional data: description, validation, and application. *Atmospheric Chemistry and Physics*, 18(9):6971–6983, 2018.

[22] Jie Sun and Zhaohua Wu. Isolating spatiotemporally local mixed Rossby-gravity waves using multi-dimensional ensemble empirical mode decomposition. *Climate Dynamics*, 54(3):1383–1405, 2020.

[23] Almut Gaßmann. Analysis of large-scale dynamics and gravity waves under shedding of inactive flow components. *Monthly Weather Review*, 147(8):2861–2876, 2019.

[24] Rafael C. Gonzalez and Richard E. Woods. *Digital image processing*. Prentice Hall, 3rd edition, 2008.

[25] Almut Gaßmann. Deviations from a general nonlinear wind balance: Local and zonal-mean perspectives. *Meteorologische Zeitschrift*, 23(5):467–481, 12 2014.

[26] Peter Névir. Ertel's vorticity theorems, the particle relabelling symmetry and the energy-vorticity theory of fluid mechanics. *Meteorologische Zeitschrift*, pages 485–498, 2004.

[27] Hans-Joachim Lange. *Die Physik des Wetters und des Klimas: ein Grundkurs zur Theorie des Systems Atmosphäre*. Reimer, 2002.

[28] Harsh Bhatia, Gregory Norgard, Valerio Pascucci, and Peer-Timo Bremer. The Helmholtz-Hodge decomposition—a survey. *IEEE Transactions on visualization and computer graphics*, 19(8):1386–1404, 2012.

[29] Mahnoosh Haghighatnasab, Mohammad Mirzaei, Ali R. Mohebalhojeh, Christoph Zülicke, and Riwal Plougonven. Application of the compressible, nonhydrostatic, balanced omega equation in estimating diabatic forcing for parameterization of inertia–gravity waves: Case study of moist baroclinic waves using WRF. *Journal of the Atmospheric Sciences*, 77(1):113–129, 2020.

[30] Nedjeljka Žagar, Damjan Jelić, Marten Blaauw, and Peter Bechtold. Energy spectra and inertia–gravity waves in global analyses. *Journal of the Atmospheric Sciences*, 74(8):2447–2466, 2017.

[31] Michael Selwyn Longuet-Higgins. The eigenfunctions of Laplace's tidal equation over a sphere. *Philosophical Transactions of the Royal Society of London. Series A, Mathematical and Physical Sciences*, 262(1132):511–607, 1968.

[32] Corwin J. Wright and John C. Gille. Detecting overlapping gravity waves using the S-Transform. *Geophysical Research Letters*, 40(9):1850–1855, 2013.

[33] Claudia Christine Stephan, Cornelia Strube, Daniel Klocke, Manfred Ern, Lars Hoffmann, Peter Preusse, and Hauke Schmidt. Intercomparison of gravity waves in global convection-permitting models. *Journal of the atmospheric sciences*, 76(9):2739–2759, 2019.

[34] Christopher G. Kruse and Ronald B. Smith. Nondissipative and dissipative momentum deposition by mountain wave events in sheared environments. *Journal of Atmospheric Sciences*, 75(8):2721–2740, 2018.

[35] Duraisamy Sundararajan. *The discrete Fourier transform: theory, algorithms and applications*. World Scientific, 2001.

[36] Vanja Blažica, Nedjeljka Žagar, Benedikt Strajnar, and Jure Cedilnik. Rotational and divergent kinetic energy in the mesoscale model ALADIN. *Tellus A: Dynamic Meteorology and Oceanography*, 65(1):18918, 2013.

[37] Geoffrey K Vallis. *Atmospheric and oceanic fluid dynamics*. Cambridge University Press, 2017.

[38] Kenneth S. Gage and Gregory D. Nastrom. Theoretical interpretation of atmospheric wavenumber spectra of wind and temperature observed by commercial aircraft during GASP. *Journal of Atmospheric Sciences*, 43(7):729–740, 1986.

[39] William C. Skamarock. Evaluating mesoscale NWP models using kinetic energy spectra. *Monthly weather review*, 132(12):3019–3032, 2004.

[40] Gregory D. Nastrom and Kenneth S. Gage. A climatology of atmospheric wavenumber spectra of wind and temperature observed by commercial aircraft. *Journal of the atmospheric sciences*, 42(9):950–960, 1985.

[41] Erik Lindborg. Can the atmospheric kinetic energy spectrum be explained by two-dimensional turbulence? *Journal of Fluid Mechanics*, 388:259–288, 1999.

[42] Chihoko Yamashita, Xinzhao Chu, Han-Li Liu, Patrick J. Espy, Graeme J. Nott, and Wentao Huang. Stratospheric gravity wave characteristics and seasonal variations observed by lidar at the South Pole and Rothera, Antarctica. *Journal of Geophysical Research: Atmospheres*, 114(D12), 2009.

[43] Carmen J. Nappo. *An introduction to atmospheric gravity waves*. Academic Press, 2013.

[44] Toshitaka Tsuda and Klemens Hocke. Vertical wave number spectrum of temperature fluctuations in the stratosphere using GPS occultation data. *Journal of the Meteorological Society of Japan. Ser. II*, 80(4B):925–938, 2002.

[45] Xian Lu, Xinzhao Chu, Weichun Fong, Cao Chen, Zhibin Yu, Brendan R. Roberts, and Adrian J. McDonald. Vertical evolution of potential energy density and vertical wave number spectrum of Antarctic gravity waves from 35 to 105 km at McMurdo (77.8 S, 166.7 E). *Journal of Geophysical Research: Atmospheres*, 120(7):2719–2737, 2015.

[46] Andrea K. Steiner and Gottfried Kirchengast. Gravity wave spectra from GPS/MET occultation observations. *Journal of Atmospheric and Oceanic Technology*, 17(4):495–503, 2000.

[47] Steven A. Smith, David C. Fritts, and Thomas E. Vanzandt. Evidence for a saturated spectrum of atmospheric gravity waves. *Journal of Atmospheric Sciences*, 44(10):1404–1410, 1987.

[48] Toshitaka Tsuda, Thomas E. VanZandt, Masahiro Mizumoto, Susumu Kato, and Shoichiro Fukao. Spectral analysis of temperature and Brunt-Väisälä frequency fluctuations observed by radiosondes. *Journal of Geophysical Research: Atmospheres*, 96(D9):17265–17278, 1991.

[49] Lotte Bierdel, Petra Friederichs, and Sabrina Bentzien. Spatial kinetic energy spectra in the convection-permitting limited-area NWP model COSMO-DE. *Meteorologische Zeitschrift*, 21(3):245, 2012.

[50] Ronald M. Errico. Spectra computed from a limited area grid. *Monthly weather review*, 113(9):1554–1562, 1985.

[51] Frauke Feser and Hans Von Storch. A spatial two-dimensional discrete filter for limited-area-model evaluation purposes. *Monthly weather review*, 133(6):1774–1786, 2005.

[52] Vanja Blažica, Nils Gustafsson, and Nedjeljka Žagar. The impact of periodization methods on the kinetic energy spectra for limited-area numerical weather prediction models. *Geoscientific Model Development*, 8(1):87–97, 2015.

[53] Remko Klaver, Rein Haarsma, Pier Luigi Vidale, and Wilco Hazeleger. Effective resolution in high resolution global atmospheric models for climate studies. *Atmospheric Science Letters*, 21(4):e952, 2020.

[54] Christopher Kruse. Personal communication.

[55] Ole Tange et al. Gnu parallel-the command-line power tool. *The USENIX Magazine*, 36(1):42–47, 2011.

[56] Sonja Gisinger, Andreas Dörnbrack, Vivien Matthias, James D. Doyle, Stephen D. Eckermann, Benedikt Ehard, Lars Hoffmann, Bernd Kaifler, Christopher G. Kruse, and Markus Rapp. Atmospheric conditions during the deep propagating gravity wave experiment (deepwave). *Monthly Weather Review*, 145(10):4249–4275, 2017.

[57] Mark A. Wieczorek and Frederik J. Simons. Localized spectral analysis on the sphere. *Geophysical Journal International*, 162(3):655–675, 2005.

[58] Jens Keiner, Stefan Kunis, and Daniel Potts. Using NFFT 3—a software library for various nonequispaced fast Fourier transforms. *ACM Transactions on Mathematical Software (TOMS)*, 36(4):1–30, 2009.

[59] Jacob T. VanderPlas. nfft. `https://github.com/jakevdp/nfft`, 2017.

[60] Toshitaka Tsuda, X. Lin, H. Hayashi, et al. Analysis of vertical wave number spectrum of atmospheric gravity waves in the stratosphere using COSMIC GPS radio occultation data. *Atmospheric Measurement Techniques*, 4(8):1627–1636, 2011.

[61] Jacob T. VanderPlas. Understanding the lomb–scargle periodogram. *The Astrophysical Journal Supplement Series*, 236(1):16, 2018.

[62] Pedro Bolgiani, Daniel Santos-Muñoz, Sergio Fernández-González, Mariano Sastre, Francisco Valero, and María Luisa Martín. Microburst detection with the WRF model: Effective resolution and forecasting indices. *Journal of Geophysical Research: Atmospheres*, 125(14):e2020JD032883, 2020.

[63] Christopher G Kruse, Ronald B Smith, and Stephen D Eckermann. The midlatitude lower-stratospheric mountain wave "valve layer". *Journal of Atmospheric Sciences*, 73(12):5081–5100, 2016.

[64] Ronald B Smith and Christopher G Kruse. A gravity wave drag matrix for complex terrain. *Journal of Atmospheric Sciences*, 75(8):2599–2613, 2018.

[65] Simon B Vosper, Annelize van Niekerk, Andrew Elvidge, Irina Sandu, and Anton Beljaars. What can we learn about orographic drag parametrisation from high-resolution models? A case study over the Rocky Mountains. *Quarterly Journal of the Royal Meteorological Society*, 146(727):979–995, 2020.

List of Figures

List of Abbreviations

DFT Discrete Fourier Transform

FFT Fast Fourier Transform

GWs Gravity Waves

MF Momentum Flux

MWD Mountain Wave Drag

NFFT Non-equispaced Fast Fourier Transform

WRF model Weather Research and Forecasting Model

A. Coordinate systems

The physical processes in the atmosphere can be described using different coordinate systems.

The mathematically simplest form of equation of motions can be obtained in an inertial coordinate system, that does not rotate with the Earth. Using such an absolute coordinate system, an interpretation of the resulting air motion is, however, more complicated.

The most commonly used description of the position of points in the atmosphere is by means of local Cartesian systems rotating with the Earth. The xy-plane of these systems is taken as the plane parallel to the tangential plane to the sphere approximating the shape of the Earth. The x-axis is considered to point from the west to the east and it is called the zonal direction. The y-axis represents the meridional direction from the south to the north. The z-axis points from the centre of the sphere upwards. In this thesis, we always use this coordinate system.

The specification of the units on the vertical axis is also variable. In so-called z-system, the axis measures the altitude. Other options are, for example, the pressure vertical coordinate, which is determined by the levels of constant pressure, or vertical coordinates that follow the terrain at least in the lower levels.

Further, we focus on the z-system, which we employ in the thesis. Because the Cartesian coordinate systems change between points, we have to derive formulas for spatial derivatives. More precisely, we will express partial derivatives of the spherical coordinates with respect to the local coordinates. Using chain rule, we can then pass from the derivatives in local coordinate system to the derivatives in the global spherical coordinates.

We denote the spherical coordinates by (r, λ, φ), where $r \in (0, \infty)$ is the radial coordinate, $\varphi \in (-90°, 90°)$ corresponds to the latitude and $\lambda \in (-180°, 180°)$ corresponds to the longitude. For a fixed pair (λ, φ), we denote the local Cartesian coordinates by (x, y, z).

First, it is clear that the derivative in the vertical direction remains unmodified, as the vertical differentiation does not operate with multiple local coordinate systems. For the derivative evaluation, we can use the fact that the vertical coordinate in the local coordinate system at a point coincides with the radial coordinate of the spherical coordinates. Mathematically, we can write

$$\frac{\partial r}{\partial x} = 0, \qquad \frac{\partial r}{\partial y} = 0, \qquad \frac{\partial r}{\partial z} = 1 \tag{A.1}$$

for every point in the space.

Because the local coordinates are similar to the spherical coordinates, we also easily see that

$$\frac{\partial \varphi}{\partial z} = 0, \qquad \frac{\partial \lambda}{\partial z} = 0, \qquad \frac{\partial \varphi}{\partial x} = 0, \qquad \frac{\partial \lambda}{\partial y} = 0. \tag{A.2}$$

The only non-trivial components of the gradient are the zonal derivative of the longitude and meridional derivative of the latitude.

We start with the meridional derivative of the latitude. The simplest derivation of the derivative is based on the understanding of the derivative as a reaction

to the infinitesimal change of a parameter. If the latitude is increased by a small angle $\Delta\varphi$, at a constant distance r in a direction of constant longitude, the coordinate y increases by $\Delta y = r\Delta\varphi$. Therefore, it holds

$$\frac{\partial\varphi}{\partial y} = \lim_{\Delta y\to 0}\frac{\Delta\varphi}{\Delta y} = \frac{1}{r}. \tag{A.3}$$

The evaluation of the derivative of the longitude is a bit more complicated. After a small change $\Delta\lambda$ of the longitude, the coordinate x again changes by $\Delta x = R\Delta\lambda$. The parameter R is, however, not the distance from the centre of the sphere as before, but the distance from an axis connecting the poles of the sphere. By the geometry, it can be expressed as $R = r\cos\varphi$. It holds,

$$\frac{\partial\lambda}{\partial x} = \lim_{\Delta x\to 0}\frac{\Delta\lambda}{\Delta x} = \lim_{\Delta x\to 0}\frac{1}{R} = \frac{1}{r\cos\varphi}. \tag{A.4}$$

Altogether, for a function $F(x, y, z) = f(\lambda(x), \varphi(y), r(z))$, we have

$$\frac{\partial}{\partial x}F(x,y,z) = \frac{1}{r(z)\cos\varphi(y)}\frac{\partial f}{\partial\lambda}\bigg|_{\lambda=\lambda(x)}, \tag{A.5a}$$

$$\frac{\partial}{\partial y}F(x,y,z) = \frac{1}{r(z)}\frac{\partial f}{\partial\varphi}\bigg|_{\varphi=\varphi(y)}, \tag{A.5b}$$

$$\frac{\partial}{\partial z}F(x,y,z) = \frac{\partial f}{\partial r}\bigg|_{r=r(z)}. \tag{A.5c}$$

Next, after the substitution of the Lamé coefficients r and $r\cos\phi$ into the general form of divergence and curl in the orthogonal coordinates, we have, for a vector-valued function $\mathbf{F} = \left(f^\lambda, f^\varphi, f^r\right)$,

$$\nabla\cdot\mathbf{F} = \frac{1}{r\cos\varphi}\left(\frac{\partial f^\lambda}{\partial\lambda} + \frac{\partial}{\partial\varphi}\left(f^\varphi\cos\varphi\right)\right) + \frac{\partial f^r}{\partial r}, \tag{A.6}$$

$$\nabla\times\mathbf{F} = \begin{pmatrix} \frac{1}{r}\left(\frac{\partial f^r}{\partial\varphi} - \frac{\partial}{\partial r}\left(rf^\varphi\right)\right) \\ \frac{1}{r\cos\varphi}\left(\frac{\partial}{\partial r}\left(f^\lambda r\cos\varphi\right) - \frac{\partial f^r}{\partial\lambda}\right) \\ \frac{1}{r\cos\varphi}\left(\frac{\partial f^\varphi}{\partial\lambda} - \frac{\partial}{\partial\varphi}\left(f^\lambda\cos\varphi\right)\right) \end{pmatrix}. \tag{A.7}$$

As in the definition of the function $\mathbf{F}$, the first component of the curl corresponds to the longitude coordinate, the second to the latitude and the third to the radial coordinate.

B. Electronic Attachment

Complete scripts used for the analysis are attached to the thesis. The enclosed .zip file has the following structure.

- The directory `spectra` contains scripts concerning the evaluation of horizontal and vertical spectra and the identification of wavelength range of GWs. The central computations apply functions in files `horizontalspectrum.py`, `verticalspectrum.py` and `locateGW-run.py`.
- Results regarding the sensitivity of the high-pass filter method were obtained using the files in directory `sensitivity_to_cutoff`. The computations are run using the script `filter_calculate_parallel.sh`. The main parts of the computations are done in files `procfiltpara-levels.ncl` and `procsubdom-levels.ncl`.
- The scripts concerning the improved high-pass filter method are located in directory `improved_filter`. The primary functions are written in the files `filter_range.py` and `dragflux.ncl`.
- The directory `active_flow` contains scripts to the active wind method. The central part of the computation is provided by the function `funfilteractive` in the file `filteractive.py`. Apart from files for plotting, the remaining files serve for data preprocessing and derivative evaluation.